INTERNATIONAL JOURNAL OF
NUMERICAL ANALYSIS AND MODELING
Volume 5, Number 3, Pages 407–440

COMPUTATIONAL ASPECTS OF LOW FREQUENCY ELECTRICAL AND ELECTROMAGNETIC TOMOGRAPHY: A REVIEW STUDY

MANUCHEHR SOLEIMANI

This paper is dedicated to my beautiful wife Leyla

Abstract. This paper studies various mathematical methods for image reconstruction in electrical impedance and magnetic induction tomography. Linear, nonlinear and semilinear methods for the inverse problems are studied. Depending on the application, one of these methods can be selected as the image reconstruction algorithm. Linear methods are suitable for low contrast imaging, and nonlinear methods are used when more accurate imaging results are required. A semilinear method can be used to preserve some properties of the nonlinear inverse solver and at the same time can have some advantages in computational time. Methods design specifically for jump in material distribution as well as dynamical imaging have been reviewed.

Key Words. Electrical impedance tomography, electrical capacitance tomography, magnetic induction tomography, magnetostatic permeability tomography, inverse problems.

1. Introduction

Imaging is the science of building 2D or 3D reconstructions from exterior measurements. The applications include medical and industrial tomography, geomagnetic prospecting, ground penetrating radar, industrial non-invasive testing and many others. Computational imaging algorithms involve the solution of large-scale inverse problems, in the form of constrained or unconstrained optimization problems. Due to the similarities in the underlying mathematical formulations of the problems, one can design algorithms which can be combined to solve large classes of applications problems.

Many imaging problems belong to the general class of the inverse problem, whose solutions are extremely sensitive to data errors (and rounding errors in the computations). An approximated solution to these problems can be computed by incorporating a priori information about the desired solution into the reconstruction model. This information can be defined explicitly, e.g., by requiring the solution to satisfy given constraints or to lie in a given subspace, or the information can be implicit, e.g., by requiring that the solution satisfies certain smoothness conditions. The algorithms that incorporate these requirements into the solution process are called *regularization algorithms*, and they usually take the form of a linear or nonlinear optimization algorithm that involves a combination of a “goodness-of-fit”

Received by the editors Jan 15, 2007 and, in revised form, September 25.
2000 *Mathematics Subject Classification.* 35R35, 49J40, 60G40.

(such as the residual norm) and a “quality measure” (such as a semi-norm) of the solution.

Low frequency electromagnetic tomography techniques (less than 20 MHz) are used to non-invasively create cross sectional images of the objects with contrasts in one or more of the passive electromagnetic properties (PEP) including conductivity, permittivity and permeability. Magnetic induction tomography (MIT) [26], [37], [46], [55], [48] is a relatively new member of the electromagnetic imaging family, which works based the eddy current in conductive objects. Image reconstruction of MIT and the three other members of this family, including magnetostatic permeability tomography (MPT) [61], [31], electrical impedance tomography (EIT) [16], [7] and electrical capacitance tomography (ECT) [82] have been studied in this paper.

EIT is the oldest member and was introduced in a medical context by Barber and Brown [6], [30]. ECT has been used for industrial process tomography applications mainly for materials with low permittivity and negligible conductivity. This review will study MIT in conductivity imaging mode and MPT for permeability imaging. EIT considered here works in electrical conductivity mode, so it is referred to as electrical resistance tomography (ERT).

In MIT and MPT a magnetic field from an excitation coil is applied to the object. MIT is based on concept of the eddy current that originates with Michael Faraday’s discovery of electromagnetic induction in 1831. In MIT, a time varying magnetic field is induced in the sample material using a magnetic coil with alternating current. This magnetic field causes an eddy current to be generated in conducting materials. These currents, in turn, produce small magnetic fields around the conducting materials. The smaller magnetic fields generally oppose the original field, which changes the transimpedance between excitation and sensing coils. Thus, by measuring the changes in transimpedance between magnetic coils as it traverses the sample, we can identify different characteristics of the sample. In MPT there is no eddy current and changes in magnetostatic fields due to the presence of a permeable object can be detected by sensing coils. The mutual inductances between excitation and sensing coil is the measurement data in MIT. In ERT electrical current is applied to the conductive body via excitation electrodes and resulting electric voltages are measured in peripheral electrodes. In ECT electric potential is applied to the excitation electrodes and capacitances are measured between pairs of electrodes. ERT requires direct contact between the imaging area and the electrodes, but MIT and MPT are fully contactless, and ECT can be used without direct contacts.

All these modalities are inherently complex. They need energization of target region, sensors, electronics, data acquisition and data processing. Induced voltages in MPT and MIT, measured voltages in ERT electrodes and measured capacitances between ECT electrodes are the data for the image reconstruction.

Image reconstruction in EIT is more advanced than for ECT and MIT. For instance, nonlinear image reconstruction methods, including most commonly used regularized Gauss-Newton, are now widely adapted for EIT imaging but not for ECT or MIT. The area of image reconstruction in ECT and MIT is still very underdeveloped. In the past few years many interesting works have been done in the area of sensor design [49], electronic design [79], [37] and basic understanding of the sensitivity maps in MIT [54]. Various types of linear reconstruction methods were used for the image reconstruction of ECT and MIT [83], [38], [8]. In ECT the main focus was to generate images by fast methods, so the computational time and complexity of a nonlinear solver could be a reason why it has not been exploited. Non-phenomenological methods (methods that do not consider and thus are not benefiting from the knowledge of the underlying physics of the measurement system) such as Neural Network and Genetic algorithm were used for image reconstruction [21], [39]. In phenomenological methods such as regularized Gauss-Newton methods one needs to numerically model the underlying physical problem. Modeling of the electric fields in ECT and ERT involves solving a Laplacian elliptic partial differential equation and scalar fields. The finite element method (FEM) is a powerful tool to solve such a problem. In MIT, further development of the image reconstruction (phenomenological method) requires computation of the general eddy current problem involving vector fields. Some simplified models were used earlier by using scalar fields in MIT [24], which were not accurate to model for higher frequency cases. Edge FEM are developed for the eddy current problem to enhance the computation of vector fields. In the past decade finite element solution of the eddy current problem has been an active area of research [9], [11], [20]. In this paper we use nodal and edge finite elements for the forward problem in ECT, MPT and MIT.

Recently, shape based reconstruction techniques have become more popular in EIT. The shape reconstruction method is intended to be applied in situations where approximate values of the parameters inside non-smooth, high-contrast structures are available, but the sizes, shapes, locations and geometry of these structures are unknown. For example, shape reconstruction method has been studied in [34], monotonicity based shape reconstruction in [76], linear sampling methods in [10], and level set method in [17]. So far most of these schemes have been applied to simulated data. The linear sampling method was applied to real measurement data in EIT and the results were reported in [29]. We have designed a narrowband level set method for the shape reconstruction. The method was applied successfully to experimental data in ECT and ERT. This shape reconstruction algorithm is a nonlinear inversion scheme, which makes use of a numerical shape propagation technique, the so-called level set technique, which originally was developed for the modeling of moving interfaces [57], [18].

The dynamical image reconstruction methods are assuming an important rule in low frequency electromagnetic imaging. Their importance is mainly because of the fact that these imaging methods are potentially very fast so that time varying and functional imaging is a very good feature. There are many different version of dynamical imaging, in this paper we only briefly review the linear Kalman filter [78], [33], [32], [63].

This paper is organized as follows. The forward problem based on finite element solution is briefly studied in section 2. The image reconstruction methods are studied in section 3 and section 4 present some sample results. Most of the image reconstruction methods explained in section 3 are general and can be used in any other tomography or inverse problem application.

2. Forward problem

The forward problem is a simulation of the observation process, when the excitation and internal material properties are given. The main equations for the forward problem in electrical and electromagnetic tomography are the Maxwell's equations. Assuming time-harmonic fields with angular frequency ω Maxwell's equations are

$$\nabla \times E = -j\omega\mu H \tag{1}$$

$$\nabla \cdot \mu H = 0 \tag{2}$$

$$\nabla \times H = (\sigma + j\omega\varepsilon)\, E + J_s \tag{3}$$

$$\nabla \cdot \varepsilon E = 0 \tag{4}$$

Here E and H are the magnetic and electric fields, σ is conductivity, μ magnetic permeability and ε permittivity. For the purpose of low frequency application in this paper we ignore the wave propagation effect [16]. Depending on the operation frequency the wave effect may need to be considered [73], [26], [84]. The forward problem in EIT and ECT can be formulated in scalar field. The forward problem in MIT involves calculation of vector field. Vector based finite element are used to solve the forward problem in MIT. Vector finite element can be defined as a member of Whitney elements, which will be discussed here.

2.1. Whitney finite elements. Edge finite element has its origin from a work by Whitney [81] in differential forms in algebraic topology. Nedlec [44], [45] is the first scientist to extend the edge finite elements in three dimensional. Since then edge finite elements have been used in various electromagnetic problems. Eddy current and magnetostatic problems are among many other electromagnetic problems that are benefited from the advancement of edge FEM [9], [20]. In [1], edge elements are used for an integral formulation for computational electromagnetic.

Edge finite element is a member of family of vector finite elements. Whitney elements are from three forms including, *0-form* defined for a scalar potential ϕ bases for first order nodal FEM, *1-form* defined for the edges and a vector potential $\mathbf{u}$ and it is the base for the edges FEM and *2-form* defined for vector field $\mathbf{u}$ and it is the base for the facet elements.

In a general any Whitney form associated with p-simplex $i_0, i_1, i_2, ..., i_p$ is

$$w_{i_0,\dots,i_p} = p! \sum_{j=1}^{p} (-1)^j \phi_{ij} d^0\phi_{i_0} \dots\dots \wedge d^0\phi_{ij-1} \wedge d^0\phi_{ij+1} \wedge \dots \wedge d^0\phi_{ip} \tag{5}$$

where ϕ_i is a piecewise linear function that has value 1 in node i and zero in other nodes of the element and d^0 is the exterior derivation. The value of a variable x can be defined by $x = \sum_i \phi_i(x) x_i$ with x_i value of x in node i and $\sum_i \phi_i(x) = 1$. The operator d^1 is for *grad* ϕ for *0-form* and d^2 is for *curl* $\mathbf{u}$ for *1-form* and d^3 is for *div* $\mathbf{u}$ for *2-form.* Based on equation (5) the lowest order is the form of degree zero defined in nodes. We have $w_i = \phi_i$, which has value 1 at node i and zero in any other nodes. The function w_i is continuous across facets. If i and j are nodes for an edge, the *1-form* belonging to this edge is $\mathbf{w}_{ij} = \phi_i \nabla \phi_j - \phi_j \nabla \phi_i$. Tangential component of $\mathbf{w}_{ij}$ is 1 along edge between nodes i, j and zero along any other edges. Tangential component of the vector field $\mathbf{w}_{ij}$ is continuous across facets. If i, j, k are nodes belonging to a face, the *2-form* belonging to the facet elements is $\mathbf{w}_{ijk} = \phi_i \nabla \phi_j \wedge \phi_k + \phi_j \nabla \phi_k \wedge s\phi_i + \phi_k \nabla \phi_i \wedge s\phi_j$. The normal component of the vector field $\mathbf{w}_{ijk}$ is continuous across facets.

Conformity of the Whitney forms is an interesting property of them. The conformity of Whitney elements is *grad* $w^0 \subset \mathbf{w}^1$ and *curl* $\mathbf{w}^1 \subset \mathbf{w}^2$ and *div* $\mathbf{w}^2 \subset w^3$, here w^3 is for scalar fields and has the same properties as *0-form.*

In this study we are working with nodal FEM based *0-form* and edge FEM based on *1-form*. Properties of nodal FEM that make them interesting for the scalar field computations are very well known, we use nodal FEM for the forward problem of ERT and ECT (scalar fields). We also use an edge finite element technique for vector field computation in eddy current and magnetostatic problems.

Edge FEM has some promising advantages compared with the more conventional nodal FEM for vector field computations. In edge FEM a vector field is represented using a basis of vector valued functions. Nodal FEM was used for the vector fields in electromagnetic. Although nodal FEM is easy and straightforward and its outcome accurate, several serious problems have been identified when the ordinary nodal-based finite elements were employed to compute vector electric or magnetic fields, most notably

- Long computation time
- Large memory requirements
- Lack of adequate gauge conditions for vector magneto-static analysis
- Satisfaction of the appropriate boundary conditions at material and conducting interfaces
- Difficulty in treating the conducting and dielectric edges and corners due to the field singularities associated with these structures
- Occurrence of non-physical or so-called spurious solutions, especially in wave-guide and scattering problems, etc.

A very important advantage of edge FEM in computational electromagnetic is their superiority in imposing physically necessary continuity properties for inter-elements, and not imposing any additional continuity. For eddy current and magnetostatic problems we developed edge FEM based on a formulation involving edge finite element modeling of the magnetic vector potential $\mathbf{A}$ [9]. The tangential component of $\mathbf{A}$ is continuous between two neighboring elements, which satisfies tangential continuity of the electric fields. The magnetic flux density is curl of magnetic vector potential, continuity of tangential component of magnetic vector potential ensures the normal continuity of magnetic flux density. Continuity of normal component of the magnetic flux density and tangential component of electric fields are two physical continuity and are satisfied by edge finite element formulation.

2.2. Forward problem in EIT. The forward problem in both ECT and EIT consists of an electrostatic approximation to Maxwell's equations. The fundamental unknown of the forward problem is the electric potential u. Given the conductivity distribution ($\gamma = \sigma$) in EIT or the permittivity distribution ($\gamma = \varepsilon$) in ECT, u is calculated in the domain of interest Ω by solving the partial differential equation

$$\nabla \cdot \gamma \nabla u = 0 \tag{6}$$

with suitable boundary conditions on $\partial\Omega$ which are further specified below. The forward problem in EIT is to predict the voltage on the sensing electrodes given the applied current to the exciting electrodes. The electric current applied to the excitation electrodes and the potential between electrodes are measured using phase sensitive detection and a differential amplifier. With metallic electrodes in contact with an aqueous solution the boundary conditions are described by the Complete Electrode Model (CEM) [72]. With current I_l on electrode E_l having contact impedance z_l, the complete electrode boundary conditions are

$$V_l = u + z_l \sigma \frac{\partial u}{\partial n} \tag{7a}$$

$$I_l = \int_{E_l} \sigma \frac{\partial u}{\partial n}\, dx^2 \tag{7b}$$

where V_l is the constant voltage on the l-th electrode, and $\sigma \partial u/\partial n = 0$ on the boundary where there is no electrode.

2.3. Forward problem in ECT. ECT sensors measure the dielectric permittivity of a sample. A typical ECT sensor comprises a circular array of 8 or 12 plate electrodes, mounted on the outside of a non-conducting pipe, surrounded by an electrical shield. For metal walled vessels, the sensor must be mounted internally, using the metal wall as the electrical shield (Figure 1.a. Figure 1 shows an experimental ECT system. Additional components include radial and axial guard electrodes, of which many configurations have been tried, to improve the quality of the measurements and hence images. It is not necessary for the electrodes to make physical contact with the specimen, so they can be used on conveyor-lines, or externally mounted to plastic piping to reduce the risk of contamination. In a typical measurement pattern the voltage is applied to one electrode and the rest of the electrodes are grounded.

The electric charge is then measured as electric current from the electrodes. The forward problem in ECT is the prediction of the collected charge on sensing electrodes for a given permittivity distribution and the electric potential on the exciting electrodes. Mathematically this amounts to solving $A_{c1}U = 0$ where the system matrix is $A = A_{c1}$. The boundary condition here is to apply the potential v_k to the active electrode and potential zero to the remaining electrodes. This is modeled by the Dirichlet boundary condition

$$u = v_k \text{ on } E_k \tag{8a}$$

$$u = 0 \text{ on } \partial V_d \backslash \cup_k E_k \tag{8b}$$

where V_d is the region containing the field (possibly an infinite region), ε is dielectric permittivity, and E_k is the $k-$th electrode, held at the potential v_k, usually attached at the surface of an insulator. The electric charge on the $k-$th electrode is given by

$$Q_k = \int\limits_{E_k} \varepsilon \frac{\partial u}{\partial n} dx^2 \tag{9}$$

where n is the inward normal on the $k-$th electrode.

2.4. Forward problem in MPT and MIT. There has been number of MIT system designed for medical and industrial applications. Systems that are sensitive to the primary field are designed by Cardiff, Manchester, Moscow group. A 5 kHz MIT system designed at the Manchester University [42] is designed for the metal flow visualization a high contrast, high conductivity imaging, the rest of the systems are designed for the low contrast low conductivity imaging. The systems insensitive to the primary magnetic fields are designed by Graz group and Karlsruhe. Figure 2 shows an experimental MIT system (20 kHz excitation frequency) designed by

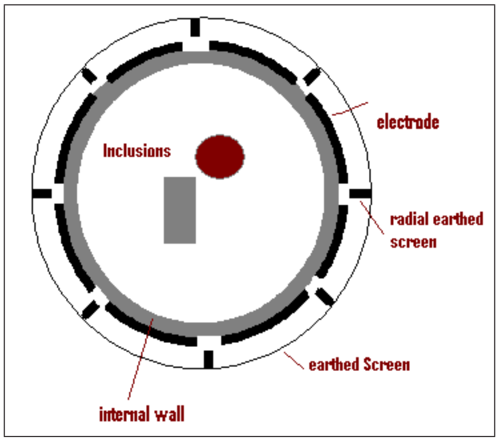

(a)

(b)

Figure 1: (a): Cross section through sensor showing electrodes and screen, (b): The PTL (Process Tomography Limited, Wilmslow, www.tomography.com) ECT system showing sensor, ECT system and host computer

Alex Korjenevesky's group in Russia [37], [38], [39]. A 16 coils MIT system (10 kHz excitation frequency) was designed and built by Cardiff MIT group [25], [79], [80]. In Bio-impedance group of Graz University of Technology Austria various interesting steps are taken to design and build MIT system and improvement of gradiameters techniques for MIT [53],[52], [56]. Multifrequency MIT system with frequency range between 50 kHz-1MHz has been designed [50]. A different gradiameter was designed for MIT measurement (4 MHz excitation frequency) by Dr Claudia Igney in the university of Karlsruhe Germany [49], [48].

Figures 3 illustrate the Graz MIT prototype and the images obtained from the system will be presented in following sections. The system mainly consists of planar gradiometers (PGRAD), low-noise amplifiers and digital signal processing for achieving high signal to noise ratio (SNR) and a excitation coil (s), EXC.

To solve the MIT imaging problem, one needs to simulate the measurement process. In MIT the general eddy current problem is an accepted approximation

Figure 2: MIT system by Alex Korjenevsky

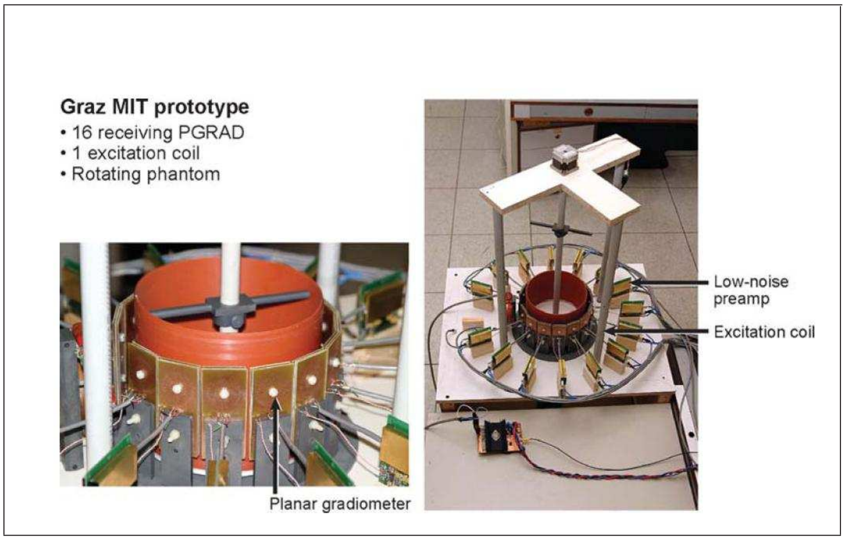

Figure 3: MIT system by Hermann Scharfetter

of the Maxwell's equations. In this section we ignore the wave propagation effect and present the author's implementation of the forward eddy current problem using edge FEM.

Edge finite element has originated from work by Whitney [81] in differential forms in algebraic topology. Nedlec [44], [45] was the first scientist to extend the edge finite elements to three dimensions. Since then edge finite elements have been used in various electromagnetic problems [11].

We use a formulation based on magnetic vector potential $\mathbf{A}$ and electric potential V. First order tetrahedral edge finite elements are employed to model the magnetic vector and the first order nodal tetrahedral elements electric scalar potential. We have developed a more general eddy current software for time harmonic eddy current modeling. For the field quantities we have $\mathbf{E} = -j\omega(\mathbf{A} + \nabla V)$ (the time derivative for electric potential is used to ensure the symmetry of linear system of equations) and $\mathbf{B} = \nabla \times \mathbf{A}$. Let us consider the quasi-static electromagnetic fields governed by

$$\nabla \times (\nu \nabla \times \mathbf{A}) + j\omega\xi(\mathbf{A} + \nabla V) = \mathtt{J}_{\mathbf{s}}. \tag{10}$$

$$j\omega\nabla \cdot (\xi(\mathbf{A} + \nabla V)) = 0 \tag{11}$$

where $\xi = \sigma + j\omega\varepsilon$ and σ , ϵ are the electric conductivity and permittivity and $\nu = 1/\mu$.

The boundary conditions of $\mathbf{A} \times \mathbf{n} = 0$ on Γ, the surface of the whole simulation domain and $\mathbf{n} \cdot (-j\omega\xi\mathbf{A} - j\omega\xi\nabla V) = 0$ on Γ_e, the surface of the eddy current region. Far field boundary conditions of normal component of magnetic field density zero are set. In edge FEM the degree of freedom is the tangential components of the vector field. The linear system of equations can be solved using the Incomplete Conjugate Gradient (ICCG) method. The electric vector potential $\mathbf{T}_s$ is defined in the coil region to represent the current in the excitation coil. Here $\nabla \times \mathbf{T}_s = \mathbf{J}_s$ and using this formulation guarantees a divergence free current source for the right hand side of equation (10) and improves the convergence of the linear solver. For simple coil shapes we are using some analytical formulation for the computation of $\mathbf{T}_s$ [9], and there is no need to mesh the coil itself. For complicated coil shapes the boundary value problem $\nabla \times (\frac{1}{\sigma}\nabla \times \mathbf{T}_s) = 0$ is solved with suitable boundary conditions in the coil region. More detailed study of the current source modeling will be presented later in this section.

Finite element discretization of (10) ,(11) using edge basis functions yields

$$\begin{aligned}\int\limits_{\Omega} (\nabla \times \mathbf{N}\frac{1}{\mu} \cdot \nabla \times \mathbf{A})dx^3 + \int\limits_{\Omega_e} (j\omega\xi\mathbf{N} \cdot (\mathbf{A} + \nabla V))dx^3 \\ = \int\limits_{\Omega_c} (\nabla \times \mathbf{N} \cdot \mathbf{T}_{\mathbf{s}})dx^3\end{aligned} \tag{12}$$

and

$$\int\limits_{\Omega_e} (j\omega\xi\nabla\phi \cdot (\mathbf{A} + \nabla V))dx^3 = 0. \tag{13}$$

where $\mathbf{N}$ is any linear combination of edge basis functions, $\mathbf{N}_{ij} = \phi_i\nabla\phi_j - \phi_j\nabla\phi_i$, ϕ is standard nodal basis, Ω is the entire region, Ω_e the eddy current region, and Ω_c the current source region. $\nabla \times \mathbf{N}$ and ∇L are constant in each elements so the integration is simple within an element. For those terms including $\mathbf{N}$ we calculate the volume integrals by Gaussian quadratures method. The Gaussian quadratures provide the flexibility of choosing not only the weighting coefficients but also the locations where the functions are evaluated. We use five Gaussian points to evaluate the integrals in each tetrahedral element.

The induced voltages (V_m) in sensing coils are calculated using

$$V_m = -j\omega \int\limits_{\Omega_c} (\mathbf{A} \cdot J_0)dx^3 \tag{14}$$

where J_0 is a virtual unitary current passing through the coil.

2.5. Sensitivity analysis. In image reconstruction it is often required to have a calculation of the sensitivity of measured data due to a small change in parameters to be imaged. The efficient sensitivity formulas are established based on sensitivity theorem in Maxwell's equations. A general study have been given in [71], [19]. The general form of the sensitivity formula for an excitation and sensing is

$$\int\limits_{\Gamma} \delta\mathbf{E}_1 \times \mathbf{H}_2 \cdot \mathbf{n}\, dx^2 = \int\limits_{\Omega} -j\omega\delta\mu\mathbf{H}_1 \cdot \mathbf{H}_2 + (\delta\sigma + j\omega\delta\varepsilon)\mathbf{E}_1 \cdot \mathbf{E}_2\, dx^3 \tag{15}$$

where the left hand side is representing sensing and excitation by surface integral on surface Γ and the right hand side is the volume integral over the perturbed region Ω. $\mathbf{H}_1$ and $\mathbf{E}_1$ are the magnetic and electric fields when sensor 1 is excited and $\mathbf{H}_2$ and $\mathbf{E}_2$ are the magnetic and electric fields when sensor 2 is excited. For each of these modalities an efficient formula can be derived to calculate the sensitivity map.

For ECT and ERT at each point in the domain the calculated sensitivity is essentially proportional to the inner product of two electric field vectors $\mathbf{E}_i \cdot \mathbf{E}_j$ at the given location. In particular, we have for ERT

$$\frac{dV_{ij}}{d\sigma}\delta\sigma = \int\limits_{\Omega} \delta\sigma\, \mathbf{E}_i \cdot \mathbf{E}_j\ dx^3 \tag{16}$$

and for ECT

$$\frac{dV_{ij}}{d\epsilon}\delta\epsilon = -\int\limits_{\Omega} \delta\epsilon\, \mathbf{E}_i \cdot \mathbf{E}_j\ dx^3. \tag{17}$$

Here, Ω is the perturbed region and $\mathbf{E}_i$ and $\mathbf{E}_j$ are the calculated electric fields of the forward problem when electrodes i and j are excited. This sensitivity formula results in an efficient method for the assembly of the Jacobian matrix. In the FEM model introduced in the previous section, we have $\mathbf{E} = -\nabla u$. For MPT the sensitivity formula for a change in permeability is proportional to $\mathbf{H}1 \cdot \mathbf{H}2$ and it is expressed as follows

$$\frac{\partial V_{ij}}{\partial \mu_k} = \frac{j\omega\nu_0}{I_i I_j \mu_k^2}[\mathbf{A}_e^i]\left(\int\limits_{\Omega_{ek}} [\nabla \times \mathbf{N}_e] \cdot [\nabla \times \mathbf{N}_e]^T dx^3\right)[\mathbf{A}_e^j]^T \tag{18}$$

where $\mathbf{N_e}$ is the edge based shape function in element e.
Equation (19) gives us the sensitivity of the voltage induced in coil i when coil j is excited with respect to μ_k relative permeability of element k. Here ν_0 is the inverse of the permeability of free space, Ω_{ek} is the volume of element number k and I_j and I_i are excitation currents for coils. And for MIT the sensitivity formula [65] for change in conductivity values is proportional to $\mathbf{E}1 \cdot \mathbf{E}2$

$$\frac{\partial V_{ij}}{\partial \sigma_k} = -\frac{\omega^2}{I_i I_j}\mathbf{A}_e^i\left(\int\limits_{\Omega_{ek}} \mathbf{N}_e \cdot {\mathbf{N}_e}^T dx^3\right)(\mathbf{A}_e^j)^T \tag{19}$$

3. Image reconstruction

The formulation of image reconstruction for one or more internal PEP characteristics from a set of boundary measurements is an example of an inverse boundary value problem. The definition of the forward problem [4] is "*Given some boundary* *conditions on the boundary $\partial\Omega$ of an object $\Omega \subset \mathbb{R}^3$, and a distribution of parameter p within Ω, find the resulting measurement set y on $\partial\Omega$*". The solution to the forward problem can be expressed in the form of a general non-linear forward operator $y = F(p)$, where $F : P \to Y$ and $F \in C^\infty(P, Y)$, where $p \in P$ and $y \in Y$. Similarly, the inverse problem may be stated as follows "*Given a distribution of PEP characteristics p and a distribution of measurements y on $\partial\Omega$ derive the PEP parameter p within Ω. This can be represented by $y = F^{-1}(p)$.*" If we have an estimated p_0 that is close to the ideal solution, then the resulting forward solution $y_0 = F(p_0)$ is close to y. Under suitable conditions one can expand the forward operator in a Taylor series. We now state sufficient conditions for the existence of a Taylor expansion. A general map $F : P \to Y$ between two Banach spaces is considered. The Fréchet derivative of F at a point p in a subset $U \subset P$ is defined as a bounded linear map by $F^{'}$ such that

$$\lim_{h\to 0} \frac{F(p+h) - F(p) - F^{'}(p)}{h} = 0 \tag{20}$$

If $F^{'}$ exists F is differentiable at p and if $F^{'}$ is continuous of p, then F is called continuously differentiable ($F \in C^1(P, Y)$). If the second derivative of F, described by $F_p^{''}$, exists we say it is twice differentiable at p, and we say $F \in C^r(P, Y)$ if $F_p^{(r)}$ is continuous. If $F \in C^r(P, Y)$ for all r we say F is smooth or $F \in C^\infty(P, Y)$. For $F \in C^r(P, Y)$ Taylor's theorem states

$$F(p+h) = F(p) + F_p^{'}(h) + (\frac{1}{2!})F_p^{''}(h,h) + ...(\frac{1}{r!})F_p^{(r)}(h,h,...,h) + o(h^r) \tag{21}$$

For $r = 1$ this reduces to (20). Here $o(h^r)$ is the Landau symbol stands for any map defined in a neighborhood of the origin of a Banach space P satisfying $\lim_{h\to 0} \dfrac{o(h^r)}{\parallel h \parallel^r} = 0$. If p_0 is an estimate close to the actual solution, the forward map can be extended by the Taylor series

$$y = F(p_0) + F_p^{'}(p_0)(p-p_0) + (\frac{1}{2!})(p-p_0)^T F_p^{''}(p_0)(p-p_0) + o(\parallel p - p_0 \parallel^2) \tag{22}$$

In the discrete case the matrix representation of $F^{'}$ in standard basis is $\mathbf{J} \in \mathbb{R}^{m\times n}$ the Jacobian matrix and $F^{''}$ represented by $\mathbf{H} \in \mathbb{R}^{m\times n}$, the Hessian (the discrete representation of the Hessian is a matrix for a single multivariable function, but for a vector value function it is a tensor). Here $\mathbf{p} \in \mathbb{R}^n$ and $\mathbf{y} \in \mathbb{R}^m$ are finite numbers of the parameter to be estimated and measured respectively. Putting $\Delta\mathbf{y} = \mathbf{y} - \mathbf{y}_0$ and $\Delta\mathbf{p} = \mathbf{p} - \mathbf{p}_0$ leads to

$$\Delta\mathbf{y} = \mathbf{J}\Delta\mathbf{p} + \Delta\mathbf{p}^T\mathbf{H}\Delta\mathbf{p} + o(\parallel \mathbf{p} - \mathbf{p}_0 \parallel^2) \tag{23}$$

Neglecting terms after the first, linear term constitutes the perturbation approach and the problem reduces to inversion of the matrix representation of $\mathbf{J}$ at $\mathbf{p}_0$. This is therefore a linear problem which may well be ill-posed, and is amenable to standard matrix inversion methods. Its success is largely dependent on how closely the initial estimate is to the correct solution, and how little effect is played by higher-order terms in equation (23). The linear methods require a different experiment that measures $\Delta\mathbf{y}$ as the difference between two states. This approach provides a means of imaging which is sensitive to the change in PEP.

3.1. Linear inverse problems. Linear reconstruction relies on the fact that for small changes, the measurement $\Delta\mathbf{y}$ can be approximated in a linear fashion with the parameter $\Delta\mathbf{p}$, which may be expressed using the Jacobian matrix $\mathbf{J}$ as

$$\Delta\mathbf{y} = \mathbf{J}\Delta\mathbf{p} + o(\| \Delta\mathbf{p} \|) \tag{24}$$

This could be interpreted as seeking either a difference image from the difference between two sets of measurement data, or it could be a step in a non-linear iterative algorithm in which the voltage difference is taken between calculated and measured data. If the number of unknowns is smaller or bigger than the number of the measurements, then the matrix $\mathbf{J}$ is not square. In such a case we can use the Moore-Penrose generalized inverse, however we must also consider the stability of the solution. In particular, measurement noise and computational errors that occur during the forward modeling means that the perturbations in object properties that can be reconstructed have also to be big enough, in order to create sufficient signal changes above the noise and computation errors. Mathematically this is described as the ill-posedness of the inverse problem. This means that the minimization of a misfit between data and model is difficult, and that small errors in the measurements or simulations can lead to large errors in the solution. For this reason, some assumptions, which incorporate as much prior information as is practical, are required.

3.1.1. Singular value decomposition: The inverse problems of finding PEP using electromagnetic tomography are ill-posed. Hadmard [27] gives a definition of an ill-posed problem saying that the solution does not exist or is not unique or is not a continuous function of the data. The third condition is one of the biggest problems in electromagnetic tomography. An arbitrary small perturbation of the data can create an arbitrarily large perturbation of the solution. Singular value decomposition (SVD) provides a means to study the ill-posedness of an inverse problem. In equation (24) in our definition of a linear inverse problem. SVD of $\mathbf{J}$ is

$$\mathbf{J} = \mathbf{U}\Sigma\mathbf{V}^T = \sum_{i=1}^{n} \mathbf{u}_i \sigma_i \mathbf{v}_i^T \tag{25}$$

here $\mathbf{U} = (\mathbf{u_1}, \mathbf{u_2}, ..., \mathbf{u_n}) \in \mathbb{R}^{m\times n}$ and $\mathbf{V} = (\mathbf{v_1}, \mathbf{v_2}, ..., \mathbf{v_n}) \in \mathbb{R}^{n\times n}$ are matrices with orthonormal columns called singular vectors, $\mathbf{U}^T\mathbf{U} = \mathbf{V}^T\mathbf{V} = \mathbf{I_n}$, and the diagonals of Σ includes the singular values, which are positive numbers $(\sigma_1, \sigma_2, ...\sigma_n)$ sorted in non-increasing order. If matrix $\mathbf{J}$ is invertible then $\Delta\mathbf{p} = \sum_{i=1}^{n} \dfrac{\mathbf{u}_i^T\Delta\mathbf{y}}{\sigma_i}\mathbf{v}_i$ is the solution to our linear problem. A plot of singular values will tell us how ill-posed a particular inverse problem is. Truncated SVD (TSVD) can be used to solve an ill-posed problem by ignoring $n-k$ number of small singular values in $\Delta\mathbf{p}_{\mathrm{ls}} = \sum_{i=1}^{k} \dfrac{\mathbf{u}_i^T\Delta\mathbf{y}}{\sigma_i}\mathbf{v}_i$ giving a least square solution $\Delta\mathbf{p}_{\mathrm{ls}}$. TSVD was used for the MIT image reconstruction and was reported in [13].

A comparison between the decay of $\|\mathbf{u}_i\Delta\mathbf{y}\|$ and σ_i's is the basis for the Picard criterion [28]. If the decay of $\|\mathbf{u}_i\Delta\mathbf{y}\|$ is faster than the decay of σ_i's then $\Delta\mathbf{p}_{\mathrm{ls}}$ will be an acceptable solution. Different measurement strategies can be compared based on Picard criteria, given one can estimate the noise level for each measurement strategy and also one can calculate the SVD for that particular measurement strategy.

If we can reduce the large decay of the singular values, in other words increase the condition number of the system of equations artificially we can have an approximation solution for the problem. By doing that we regularize the ill-posed problem. For example replacing σ_i by $\sigma_i^{\mathrm{new}} = \dfrac{\sigma_i^2 + \alpha^2}{\sigma_i}$ we have $\Delta p_{\mathrm{ls}} = \sum_{i=1}^{n} \dfrac{\mathbf{u}_i^T \Delta \mathbf{y}}{\sigma_i^{\mathrm{new}}} \mathbf{v}_i$ that can be solved in a stable manner. Choosing a small value of α has a small effect on lager singular values, whilst at the same time smaller singular values are contributing in the solution in stabilized way. Because of the regularization the contribution, the smaller singular values in the solution are not the exact reflection of those singular values of the components in the measurements.

3.1.2. Underdetermined and overdetermined: We are looking to find $\Delta\mathbf{p}$ in the interior given measured data $\Delta\mathbf{y}$ on the boundary. Solving the inverse problem by minimizing

$$\Delta\mathbf{p}_{ls} = \mathrm{argmin}\,(\parallel \Delta\mathbf{y} - \mathbf{J}\Delta\mathbf{p} \parallel^2) \tag{26}$$

This is the so called *output least squares* approach. If $\mathbf{J}$ is a square matrix $\Delta\mathbf{p} = \mathbf{J}^{-1}\Delta\mathbf{y}$. When $\mathbf{J}$ is not square we need

$$\Delta\mathbf{p} = \mathbf{J}^{+}\Delta\mathbf{y} \tag{27}$$

Where $\mathbf{J}^+ = \mathbf{J}^T(\mathbf{J}\mathbf{J}^T)^{-1}$ in the underdetermined case and $\mathbf{J}^+ = (\mathbf{J}^T\mathbf{J})^{-1}(\mathbf{J}^T)$ for the overdetermined case. In many cases the image reconstruction problem is an underdetermined problem.

3.1.3. Tikhonov regularization: A big change in $\Delta\mathbf{p}$ makes a small change on the measurements. This means that the optimization in (26) fails to produce a correct result. In order to overcome the ill-posedness we need to regularize, imposing additional information about the solution. A penalty term can be added to the optimization problem

$$\Delta\mathbf{p}_{GT} = \mathrm{argmin}\ \parallel \Delta\mathbf{y} - \mathbf{J}\Delta\mathbf{p} \parallel^2 + \alpha^2 \parallel \mathbf{R}(\Delta\mathbf{p} - \Delta\mathbf{p_0}) \parallel^2 \tag{28}$$

A simple choice for the regularization penalty term is the Tikhonov regularization. The aim of this regularization is to dampen the contribution of smaller singular values in the solution. The matrix $\mathbf{R}$ is a regularization matrix which penalizes extreme changes in parameter $\mathbf{p}$ removing the instability in the reconstruction at the cost of producing artificially smooth images. TSVD achieves this goal by explicitly removing those smaller singular values. In Tikhonov regularization, by adding a penalty term the effect of smaller singular values are dampened in an implicit way. The parameter α controls the trade-off between fitting the data and violating the prior assumption.

The regularization would mean making the resulting linear system better conditioned. But it does not necessarily mean having a solution that is acceptable. An acceptable solution can be achieved by considering the realistic situation in the measurement as well as the material side. In the measurement side we would like to include the reality of the electronic noise and any other sources of errors either in the measurement or in the model. In the parameter side, a good initial guess is a good regularization which means $\parallel \Delta\mathbf{p} - \Delta\mathbf{p_0} \parallel$ is small. The inversion step in discrete form is

$$\Delta\mathbf{p} = (\mathbf{J}^T\mathbf{J} + \alpha^2\mathbf{R}^T\mathbf{R})^{-1}(\mathbf{J}^T\Delta\mathbf{y} + \alpha^2\mathbf{R}^T\mathbf{R}\Delta\mathbf{p_0}) \tag{29}$$

A simple form is the standard Tikhonov where $\mathbf{R} = \mathbf{I}$ and assuming $\Delta p_0 = 0$

$$\Delta\mathbf{p} = (\mathbf{J}^T\mathbf{J} + \alpha^2\mathbf{I})^{-1}(\mathbf{J}^T\Delta\mathbf{y}) \tag{30}$$

3.1.4. Generalized SVD:. Generalized SVD (GSVD) of a pair of matrices $\mathbf{J} \in \mathbb{R}^{m\times k}$ and $\mathbf{R} \in \mathbb{R}^{n\times k}$. The singular values of $\mathbf{J}^T\mathbf{J}$ and $\mathbf{R}^T\mathbf{R}$ are the square of singular values of $\mathbf{J}$ and $\mathbf{R}$. GSVD is a good tool to analyze the regularized system. Here $m < k$ and $n = k$, and the pair can be decomposed to $\mathbf{U}, \mathbf{V}, \Theta, \mathbf{C}, \mathbf{S} \in \mathbb{R}^{k\times k}$ where $[\mathbf{J},\ \mathbf{0}] = \mathbf{U}\mathbf{C}\Theta^{-1}$, $\mathbf{R} = \mathbf{V}\mathbf{S}\Theta^{-1}$, here $\mathbf{U}$ and $\mathbf{V}$ are orthogonal and Θ is square and nonsingular and $\mathbf{C}$ and $\mathbf{S}$ are diagonal matrices of the singular values of $\mathbf{J}$ and $\mathbf{R}$. Given $\lambda_i = \dfrac{\mathbf{C}_{ii}}{\mathbf{S}_{ii}}$ for $i = 1, 2...k$, and $\Delta\mathbf{y}^f = \Delta\mathbf{y},\ 0] \in \mathbb{R}^k$ the general Tikhonov solution can be written as $\Delta\mathbf{p} = \sum_{i=k-n}^{k} \xi_i \dfrac{\mathbf{u}_i^T\Delta\mathbf{y^f}}{\lambda_i}\theta_i$, and ξ_i is the filter factor and $\xi_i = \dfrac{\lambda_i^2}{\lambda_i^2 + \alpha^2}$. This factor tends to zero when λ_i is very small compared to α, which means rejecting the effect of smaller singular values in the solution. The filter factor in TSVD is 1 for selected singular values and zero for the rejected ones. And for standard Tikhonov the filter factor is $\xi_i = \dfrac{\sigma_i}{\sigma_i^2 + \alpha^2}$ where σ_i is *i-th* singular value of matrix $\mathbf{J}$. The Picard criteria from GSVD information is also useful for analyzing the regularized system with the expected noise level in measurement data [28].

3.1.5. Other methods: In Newton one step reconstruction (NOSER) [15] the regularization matrix is $\mathbf{R}^T\mathbf{R} = \mathrm{diag}(\mathbf{J}^T\mathbf{J})$. Replacing σ_i to $\sigma_i^{\mathrm{new}} = \dfrac{\sigma_i^2 + \alpha^2 l_i}{\sigma_i}$, and l_i is diagonal elements of $\mathbf{J}$. We have $\Delta\mathbf{p_{ls}} = \sum_{i=1}^{n} \dfrac{\mathbf{u}_i^T\Delta\mathbf{y}}{\sigma_i^{\mathrm{new}}} v_i$ that can be solved in a stable manner.

Krylov subspace methods such as preconditioned conjugate gradient (PCG) also act as an implicit regularization for the ill-posed inverse problem and can be efficient when used for the large scale problems. A simpler iterative algorithm is the Landweber iteration scheme used in ECT image reconstruction. Let us consider Landweber's iterations as give by the formulation

$$\Delta\mathbf{p_{i+1}} = \Delta\mathbf{p_i} + \lambda\mathbf{J}^T(\Delta\mathbf{y} - \mathbf{J}\Delta\mathbf{p_i}) \tag{31}$$

where the fixed parameter λ is a relaxation parameter. If $\parallel \mathbf{I} - \lambda\mathbf{J}^T\mathbf{J} \parallel_2^2 < 1$ or $0 << 2\|\mathbf{J}^T\mathbf{J}\|_2^2$ the method will converge. The method can be expressed as an SVD filter with the filter factor for iteration i is $\xi_i = \dfrac{(1 - (1 - \lambda\sigma_i^2))^i}{\sigma_i}$. A hybrid method is

$$\Delta\mathbf{p_{i+1}} = \Delta\mathbf{p_i} + \lambda(\mathbf{J}^T\mathbf{J} + \alpha^2\mathbf{R}^T\,\mathbf{R})^{-1}(\mathbf{J}^T)(\Delta\mathbf{y} - \mathbf{J}\Delta\mathbf{p_i}) \tag{32}$$

This is an algorithm for finding the nearest local minimum of a function which presupposes that the gradient of the function can be computed. The method of steepest descent is also called the gradient descent method. The steepest descent method is given by iteration $\Delta\mathbf{p_{i+1}} = \Delta\mathbf{p_i} + \lambda_i \mathbf{J}^T(\Delta\mathbf{y} - \mathbf{J}\Delta\mathbf{p_i})$ and in iteration i we calculate $\lambda_i = \dfrac{\| \mathbf{J}^T(\Delta\mathbf{y} - \mathbf{J}\Delta\mathbf{p_i}) \|}{\| \mathbf{J}\mathbf{J}^T(\Delta\mathbf{y} - \mathbf{J}\Delta\mathbf{p_i}) \|}$.

3.2. Nonlinear inverse problems. Nonlinear methods are suitable to reconstruct the absolute values whereas linear methods are useful for difference imaging. First we begin from minimization of the residual error

$$g(p) = \frac{1}{2} \| y - F(p) \|^2 \tag{33}$$

Consider $D(p) = y - F(p)$. Here gradient of g is $\nabla g(p) = F^{'}(p)(y - F(p))$.

$$D(p+h) = D(p) + D'(p)h + \left(\frac{1}{2}\right) F^{''}(p)h^2 + o(\| h^2 \|) \tag{34}$$

Newton's method began as a method to approximate the roots of functions, equivalently, here solutions to equation $g(p) = 0$. A Newton-Raphson iteration is $p_{i+1} = p_i + \nabla g(p_i)$, gradient of g can be used to optimize $g(p)$ by $D(p+h) \approx 0$. By ignoring second order term we have $D(p+h) = D(p) + D^{'}(p)h$ so $D^{'}(p)h = D(p+h) - D(p)$. The iterations are in a way that $D(p+h) \to 0$, which means $h = D^{'}(p)^{-1}D(p)$. Therefore Newton-Raphson iterations can be written $p_{i+1} = p_i + F'(p_i)^{-1}(y - F(p_i))$. The Hessian for the function g can be calculated

$$H(p) = D^{'}(p)^T D^{'}(p) + D^{''}(p)D(p) = F^{'}(p)^T F^{'}(p) + \sum_{j=1}^{k} F_j^{''}(p)(F_j(p) - y_j) \tag{35}$$

By ignoring second derivative term in the Hessian the Gauss-Newton iteration can be written $p_{i+1} = p_i - H(p_i)^{-1}\nabla g(p_i)$. The Gauss-Newton method is a standard optimization technique for well-posed problems. By replacing Hessian with identity, we can build a nonlinear conjugate gradient (NLCG) algorithm with regularization [3]

```
Data: Measurement data
Result: Solution of the nonlinear inverse problem
initialization;
for i=1,2,... do
    if $\| \nabla g(p_i) \|^2 < tol$ then
        break ;
    else
        $\beta_i = \dfrac{\| \nabla g(p_i) \|^2}{\| \nabla g(p_{i-1}) \|^2}$ ;
        $\Lambda_i = -(W\nabla g(p_i) + \alpha^2 I) + \beta_i \Lambda_{i-1}$ ;
    end
    line search for $\lambda_i$ ;
    $p_{i+1} = p_i + \lambda_i \Lambda_i$;
end
```

Algorithm 1: Nonlinear CG algorithm

here *tol* is the tolerance and α is the regularization parameter. A weighting function W can be used to improve the efficiency of NLCG and was applied to the EIT problem. NLCG does not require calculation of the Hessian and using adjoint formulation one can calculate the ∇g efficiently.

A nonlinear Landweber can be described by iteration $p_{i+1} = p_i + \lambda F'(p_i)(y - F(p_i))$. In the regularized Gauss-Newton method the second order term in the Hessian is approximated. The regularized optimization is to find p, given p_0 as the initial guess, $R(p)$ is the regularization function, and we also include regularization parameter α we have $g(p) = \frac{1}{2} \parallel y - F(p) \parallel^2 + \alpha^2 R(p)$

For regularized Gauss-Newton the iteration steps are $p_{i+1} = p_i - H(p_i)^{-1}\nabla g(p_i)$, where $H(p_i) = F^{'}(p_i)^T F^{'}(p_i) + \alpha^2 R^{''}(p_i)$, where H is the modified Hessian here and $R(p)$ is regularization function and $\nabla g(p_i) = F^{'}(p_i)(F(p_i) - y) + \alpha^2 R^{'}(p_i)$. Here $R'(p_i)$ and $R^{''}(p_i)$ are the first and second derivatives of $R(p)$ with respect to p_i. The regularized Gauss-Newton (GN) algorithm is as follows:

```
Data: Measurement data
Result: Solution of the nonlinear inverse problem
Initialization ;
for i=1,2,... do
    if Stopping criteria is satisfied then
        break;
    else
        Material distribution $\mathbf{p}_i$ in step i ;
        Calculate the forward model $\mathbf{F}(\mathbf{p}_i)$ ;
        Calculate the sensitivity term $\mathbf{F}^{'}(\mathbf{p}_i)$ ;
        Choose regularization parameter $\alpha$ ;
        Compute gradient by $\nabla g(\mathbf{p}_i) = \mathbf{F}^{'}(\mathbf{p}_i)(\mathbf{F}(\mathbf{p}_i) - \mathbf{y}) + \alpha^2 R^{'}(\mathbf{p}_i)$ ;
        Compute G-N approximation of $\mathbf{H}$ by
        $\mathbf{H}(\mathbf{p}_i) = \mathbf{F}(\mathbf{p}_i)^{'}\mathbf{F}(\mathbf{p}_i) + \alpha^2 R^{''}(\mathbf{p}_i)$ ;
        Calculate $\delta\mathbf{p}_i = -\mathbf{H}(\mathbf{p}_i)^{-1}\nabla g(\mathbf{p}_i)$ ;
        Update the material distribution $\mathbf{p}_{i+1} = \mathbf{p}_i + \lambda_i \delta\mathbf{p}_i$, here $\lambda_i$ is
        the step size ;
    end
end
```

Algorithm 2: G-N algorithm

3.2.1. Linearized Tikhonov steps: Let's consider the generalized Tikhonov regularization

$$p = \operatorname{argmin}(\|\mathbf{F}(\mathbf{p}) - \mathbf{Y_m}\|^2 + \alpha^2\|\mathbf{R}(\mathbf{p} - \mathbf{p}_0)\|^2) \tag{36}$$

Iin discrete form we have iteration steps such that

$$\Delta\mathbf{p_i} = \left(\mathbf{J_i}^T\mathbf{J_i} + \alpha^2\mathbf{L}^T\mathbf{L}\right)^{-1}\mathbf{J_i}^T\left((\mathbf{Y_m} - \mathbf{F}\left(\mathbf{p_i}\right)) - \alpha^2\mathbf{R}^T\mathbf{R}(\mathbf{p_i} - \mathbf{p_0})\right) \tag{37}$$

For $i = 1$ this is a linear reconstruction algorithm. Here $\mathbf{J_i}$ is the Jacobian calculated for the inverse parameter $\mathbf{p_i}$, $\mathbf{Y}_m$ is the vector of measurements and the forward solution $\mathbf{F}\left(\mathbf{p_i}\right)$ is the predicted measurement from the forward model with parameter $\mathbf{p_i}$. There are methods to find the best regularization parameter for linear problems, for example *L-Curve* method [28]. Morozov's stopping criteria has been used to stop the iterations [43]. The iteration will stop when $\parallel \mathbf{F}(\mathbf{p}_i) - \mathbf{Y_m} \parallel < \epsilon$, where ϵ is the noise level estimated in measurement system.

3.3. Semi-linear methods. In the Newton-Kantorovich [36] the same Jacobian matrix is used in all iterations. In a sense that the forward problems are solved in each iteration but the Jacobian matrix is not updated, the method is a semilinear method. With the aim of speeding up Newton type algorithms the Broyden Quasi-Newton (BQN) method has been studied for EIT [40] and capacitance tomography by [67].

In the BQN technique one needs to solve the forward problem in each step and the inverse of the Jacobian matrix can be updated with direct formula as follows. If F is the forward map and $\mathbf{Y}_m$ is the measurement capacitance, we define $\mathbf{D} = \mathbf{F} - \mathbf{Y}_m$ and $\gamma = \mathbf{D}_{i+1} - \mathbf{D}_i$ and $\Delta\mathbf{p}_{i+1} = \mathbf{p}_i - \mathbf{p}_{i+1}$. The material distribution that best describes the actual solution is the one that makes $\mathbf{D} \approx 0$. The solution for this particular permittivity can be found using the iterative equation

$$\mathbf{p}_{i+1} = \mathbf{p}_i + \mathbf{H}_i \mathbf{D}_i \tag{38}$$

We start with an initial guess, and update the solution for each iteration. $\mathbf{H}_i$ is an approximation of the inverse of the Jacobian matrix related to permittivity distribution $\mathbf{p}_i$. Instead of calculating the Jacobian matrix and solving a linear system of equation in each iteration, the matrix $\mathbf{H}$ can be updated with $O(n^2)$ operations, n is the number of pixels of the image as follow

$$\mathbf{H}_{i+1} = \mathbf{H}_i + \frac{(\Delta\mathbf{p} - \mathbf{H}_i\gamma_i)\Delta\mathbf{p}_i^T\mathbf{H}_i}{\Delta\mathbf{p}^T\mathbf{H}_i\gamma_i} \tag{39}$$

It has been shown that the method has super-linear convergence and that the set of matrices $\mathbf{H}_i, i = 1, 2, 3, ...$ converges to $\mathbf{H}^{true}$ (The inverse of the Jacobian matrix at the point $\mathbf{p}^{true}$ where $\mathbf{D} = 0$ is satisfied). The initial guess for the BQN method is important to the convergence. If we start close to the solution the BQN converges fast. If the initial guess is far from the solution, the BQN may not converge. A mixed regularized Gauss-Newton and BQN are used for the high contrast imaging, where the first few steps are using regularized Gauss-Newton and when we are approaching the solution we can benefit from faster BQN iteration [40].

3.4. Methods for material with jump changes.

3.4.1. Total variation regularization: Although Tikhonov type regularization provides a good method to reconstruct smooth parameters both in terms of contrast and shape, it fails to reconstruct the sharp edges and absolute values for the high contrast case. TV regularization is a more suitable method for both sharp edges and high contrast. Using TV regularization to reconstruct the sharp edges has been discussed in [66] for ECT using experimental data. Complicated shape objects such as rectangular shape and cross shape objects, which has sharp edges has been reconstructed successfully using TV scheme. The recovery of sharp edges in MIT using TV regularization is similar to the ECT problem. In other words, the TV functional is used to encourage blocky images as a regularized solution. The TV functional of a continuum σ

$$G_{\mathrm{TV}}(\sigma) = \int\limits_{\Omega_{\mathrm{in}}} |\nabla\sigma(x)| dx \tag{40}$$

Here we choose to use minimum total variation method. Let's the area of each facet i between two voxels be q_i and $i = 1, 2, .., I$. The k-th row of the matrix $\mathbf{S} \in \mathbb{R}^{I \times P}$

(here I is number of facets and P is number of tetrahedral elements) is chosen to be $\mathbf{S}_k = [0, ...0, 1, ..., -1, 0, ..., 0]$, where 1 and -1 occur in the columns related to the tetrahedron with common facets k. Each row of $\mathbf{S}_k$ has been weighted with the surface area of q_k of the facet k, where $\mathbf{R}_{\mathrm{TV}} = \mathbf{S}^T\mathbf{QS}$ is the regularization matrix and $\mathbf{Q}$ is a diagonal matrix with $\mathbf{Q}(k,k) = q_k$. The term $\| \mathbf{R}_{\mathrm{TV}}\sigma \|_1$ gives an approximation to the total variation of the distribution σ. In [64], TV regularization was applied to the experimental data of industrial MIT, a good separation between highly conductive inclusions could not be achieved by smoothing Tikhonov regularization and was achieved by TV method.

3.4.2. Level set method: In the level set technique [58], [41] the boundaries of the shapes are represented by the zero level set of a level set function f. More specifically, if D is the inclusion with conductivity (or permittivity) p_{int} embedded in a background with conductivity (or permittivity) p_{ext}, the boundary of the inclusion, which is also an interface between two materials, is given by

$$\partial D := \{r : f(r) = 0\} \tag{41}$$

where the image parameter at each point r is

$$p(r) = \begin{cases} p_{int} & \{r : f(r) < 0\} \\ p_{ext} & \{r : f(r) > 0\} \end{cases} \tag{42}$$

If we change this level set function for example by adding an update, we move the shapes accordingly. This relation is used in the level set technique when constructing updates δf to a given level set function f such that the shapes are deformed in a way which reduces a given cost function.

We want to combine well-known and very efficient optimization techniques (in particular the general idea of a Gauss-Newton approach) with our newly developed shape based inversion approach. Using optimization strategies for the shape inversion as an alternative to a shape evolution approach was already suggested in the early paper by Santosa [51]. In order to mathematically derive this new optimization scheme for our situation, we will denote the mapping which assigns to a given level set function f_D the corresponding parameter distribution p by $p = \Phi(f_D)$. The parameter distribution p has the same meaning as in the traditional Gauss-Newton inversion scheme. The only difference is that in the shape based situation it is considered as having only two values, namely an interior value and an exterior value. (Certainly, this assumption can be generalized by allowing these interior and exterior values to be smoothly varying functions, separated by the interface. We will not consider this extension here.) Moreover, in our new approach it will only be an intermediate parameter, linking the data finally to the new basic unknown of the inverse problem, namely the level set function f_D.

Having defined this mapping Φ, we can now replace the iterated parameter p_n by $p_n = \Phi(f_{D^n}) = \Phi(f^n)$. Instead of the classical pixel/voxel based forward mapping $F(p)$ we need to consider now in the new Gauss-Newton type approach the combined mapping $G(f) = F(\Phi(f))$.

If we perturb the latest best guess for the level set function f by some small correction δf, the linearized response in the data will be

$$G^{'}[f]\delta f = F^{'}[\Phi(f)]\Phi^{'}[f]\delta f \tag{43}$$

according to the chain rule. Plugging this into a Gauss-Newton type algorithm, and using an update formula for the level set function as it was derived and discussed in [51], we try to calculate successive updates δf for the level set function such that the shape corresponding to the final level set function fits the simulated measurements to the given data as accurately as possible. The discretized form of $\Phi^{'}[\Psi]$ is described by $\mathbf{K}$, and the Jacobian of $\mathbf{G}$ by $\mathbf{B}$. Then, the new Gauss-Newton update is

$$\Psi_{n+1} = \Psi_n + \lambda_n \left(\mathbf{B}_n^T \mathbf{B}_n + \alpha^2 \mathbf{L}^T \mathbf{L}\right)^{-1} \mathbf{B}_n^T \left(\mathbf{A}_d - \mathbf{G}\left(\Psi_n\right)\right) \tag{44}$$

with

$$\mathbf{B} = \mathbf{JK}, \qquad \mathbf{B}^T = \mathbf{K}^T \mathbf{J}^T, \qquad \mathbf{B}^T \mathbf{B} = \mathbf{K}^T \mathbf{J}^T \mathbf{JK}. \tag{45}$$

Here $\mathbf{L}$ is the regularization matrix and has been chosen as identity matrix in this paper. Notice that (45) implies that $\mathbf{B}^T\mathbf{B}$ can be restricted to be defined only on the narrowband, since both $\mathbf{K}$ and $\mathbf{K}^T$ contain discretized versions of $\chi_\rho(r)$, $\mathbf{A}_d$ is measurement data, α is the regularization parameter and λ_n is the step-size parameter. Here χ_ρ, is the indicator function of a small narrow band of half-width ρ centered at ∂D. This is like a band pass filter in space. The iteration is terminated using Morozov's criterion: when the residual error falls below the measurement accuracy [43].

With an iterative method using an update formula for level set function we try to fit the measurement data to the simulated ones. Based on the assumption that the number of elements: N, number of measurements: M, and the number of Nodes: P. The inclusion is D and the boundary of the inclusion is ∂D. The numerical implementation is as follows

- $N \times 1$ vector containing level set function Ψ which has the same format as the real conductivity. This is assigned to the center of each element. So p_k is the conductivity of element number k and Ψ_k is defined for $k = 1, 2, ..., N$. Where $p_k = p_{int}$ and $\Psi_k < 0$ for inclusion and $p_k = p_{ext}$ and $\Psi_k > 0$ for back ground.
- Beginning with an initial guess for level set such as an spherical inclusion with level set function $\Psi_k = (X - X_0)^2 + (Y - Y_0)^2 + (Z - Z_0)^2 - r^2$ where (X_0, Y_0, Z_0) are cartesian coordinates of the center and r is radius of the sphere.
- Search for zero level set $\Psi_k = 0$, for each element $k = 1, 2, ..., N$ compare sign of Ψ_k with sign of the nearest neighbors. If Ψ_k changes its sign, choose the center of that element as an interface.
- Narrowband function, requires a $N \times 1$ vector indication narrow bands, those which are in narrowband get 1 and the others 0.
- Updating the $\delta\Psi$ level set using equation (44).
- Optionally smooth the level set function.
- Calculate the conductivity in step n as $p_n = p_{int}$ when $\Psi < 0$ and $p_n = p_{ext}$ when $\Psi > 0$.
- Stop the iteration if the residual error is smaller than the noise level Visualization the shape results

3.4.3. Monotonicity method: Monotonicity based technique was introduced for EIT shape reconstruction [76]. The resistance matrix in EIT has the monotonicity property and the inversion method has been designed based on that [74].It is possible to show that the second order moment of the impedance matrix in MIT has the monotonicity property [74], [68], [75]

$$Re\left\{\mathbf{Z}_0\left(j\omega\right) - \mathbf{Z}_\eta\left(j\omega\right)\right\} = \omega^2 \mathbf{P}_\eta^{(2)} + o\left(\omega^4\right), \ \omega \rightarrow 0 \tag{46}$$

where Re is for real part of a complex number, ω is the angular frequency, $Z_0(j\omega)$ is the impedance matrix when the conductor is not present and $\mathbf{Z}_\eta(j\omega)$ is the impedance matrix when a conductor of resistivity η is present. The main property of the second order moment is its monotonicity

$$\eta_1(\mathbf{x}) \geq \eta_2(\mathbf{x}) \quad \text{in } \Omega_e \Rightarrow \mathbf{P}_1^{(2)} \geq \mathbf{P}_2^{(2)} \tag{47}$$

where $\mathbf{P}_k^{(2)}$ is the second order moment associated to the conductivity $1/\eta_k$.

For two phases problem, (47) can be recast as

$$D_\beta \subseteq D_\alpha \subseteq \Omega_e \Rightarrow \mathbf{P}_\alpha^{(2)} \geq \mathbf{P}_\beta^{(2)} \tag{48}$$

where Ω_e is the eddy current region, $\mathbf{P}_\gamma^{(2)}$, for $\gamma \in \{\alpha, \beta\}$ is the second order moment related to a resistivity η_γ defined as

$$\eta_\gamma(\mathbf{x}) = \begin{cases} \eta_i \ \forall \mathbf{x} \in D_\gamma \\ \eta_b \ \forall \mathbf{x} \in \Omega_e / D_\gamma \end{cases} \tag{49}$$

The monotonicity (47) and (48) have been proved for a numerical model, however, it is possible to show that they hold also for the actual second order moment. The monotonicity satisfied in MIT involves $\mathbf{P}^{(2)}$ whereas we measure the impedance matrix $\delta\mathbf{Z}(j\omega)$ at the angular frequencies $\omega_1, \ldots, \omega_v$. Therefore, we need a preliminary step to apply the non-iterative inversion method aimed to extract $\mathbf{P}^{(2)}$ from the measured data. A detailed description of this calculation can be seen in [74].

Here we briefly summarize the monotonicity shape reconstruction method based on second order moment data. The inversion method presented (see [76, 75] for details) can be applied to two-phase problems and is a quantitative non-iterative inversion method requiring the solution of a number of direct problems growing as $O(N)$ or less [75]. We obtain the proposition at the basis of the inversion method

$$\mathbf{P}_{\eta_1}^{(2)} \not\geq \mathbf{P}_{\eta_2}^{(2)} \Rightarrow D_1 \not\subseteq D_2. \tag{50}$$

Proposition (50) is a criterion allowing us to exclude the possibility that D_1 is contained in D_2 by using the knowledge of the matrices $\mathbf{P}_{\eta_1}^{(2)}$ and $\mathbf{P}_{\eta_2}^{(2)}$. Notice that (50) does not exclude that D_1 and D_2 are overlapped, i.e. does not exclude the case $D_1 \cap D_2 \neq \emptyset$ where $\emptyset$ is the void set. Let us initially assume that the measured resistance matrix $\tilde{\mathbf{P}}^{(2)}$ is noise free ($\tilde{\mathbf{P}}^{(2)}$) corresponds to an unknown anomaly occupying region V), that the conductive domain Ω_c is divided into N "small" non-overlapped parts $\Omega_1, \ldots, \Omega_N$ and that the anomalous region V is union of some Ω_k's. Proposition (50) yields in a rather natural way to the inversion method. In fact, to understand if a given Ω_k is part of V, we need to compute the largest and smallest eigenvalues of the matrix $\mathbf{P}_{\Omega_k}^{(2)} - \tilde{\mathbf{P}}^{(2)}$. If the eigenvalues have opposite sign, then $\mathbf{P}_{\Omega_k}^{(2)} - \tilde{\mathbf{P}}^{(2)}$ is not positive definite and, thanks to (50) applied to $\tilde{\mathbf{P}}^{(2)}$ (V) and $\mathbf{P}_{\Omega_k}^{(2)}$ (Ω_k) it follows that $\Omega_k V$. Since, by construction, Ω_k is either contained in V or external (we are assuming that V is union of some Ω_j's), it follows that Ω_k cannot be included in V. Therefore, the reconstruction V_{ext} is given by the union of those Ω_k's such that $\mathbf{P}_{\Omega_k}^{(2)} - \tilde{\mathbf{P}}^{(2)}$ is positive semi-definite.

It is worth noting that criterion (50) is a sufficient condition to exclude Ω_k from V. In other words, $V \subseteq V_{ext}$. Criterion (50) can also be used to identify some of the extra Ω_k's contained in V_{ext}. Indeed, if Ω_k is contained in V_{ext} but not in

V, then $V \subseteq V_{ext} \backslash \Omega_k$ and, therefore, $\tilde{\mathbf{P}}^{(2)} - \mathbf{P}^{(2)}_{V_{ext} \backslash \Omega_k}$ is a positive semi-definite matrix. Thus, when $\tilde{\mathbf{P}}^{(2)} - \mathbf{P}^{(2)}_{V_{ext} \backslash \Omega_k}$ is not a positive semi-definite matrix, we can infer that Ω_k is surely part of V. Defining V_{int} as the union of those Ω_k such that $\tilde{\mathbf{P}}^{(2)} - \mathbf{P}^{(2)}_{V_{ext} \backslash \Omega_k}$ is not a positive semi-definite matrix, we have, by construction, that $V_{int} \subseteq V$.

In practice, the noise affecting the measurements, the model error introduced when we assume that V is union of some Ω_k, the error made in estimating $\tilde{\mathbf{P}}^{(2)}$ from the measured data, make the problem more complicated. Some eigenvalues, among which the ones having the smaller absolute value, may be completely contaminated by these source of error. Therefore, testing if a matrix as $\mathbf{P}^{(2)}_{\Omega_k} - \tilde{\mathbf{P}}^{(2)}$ or $\tilde{\mathbf{P}}^{(2)} - \mathbf{P}^{(2)}_{V_{ext} \backslash \Omega_k}$ is positive semi-definite or not, may give completely wrong information. To overcome the problem, it is appropriate to introduce a way to quantify how much a matrix is "close" to be a positive semi-definite matrix. A possible choice, that resulted to be very effective [76]-[75], consists of introducing a sign index defined on an arbitrary square, symmetrical and non-vanishing matrix $\mathbf{A}$ as

$$f(\mathbf{A}) = \frac{\sum_i \lambda_i}{\sum_i |\lambda_i|} \tag{51}$$

where λ_i is the $i-$th eigenvalue of the given matrix $\mathbf{A}$. We notice that $|f(\mathbf{A})| \leq 1$ and $f(\mathbf{A}) = 1$ ($f(\mathbf{A}) = -1$) if and inly if the matrix is positive (negative) semi-definite.

To compute V_{ext} we associate to each Ω_k the number $s_k = f\left(\mathbf{P}^{(2)}_{\Omega_k} - \tilde{\mathbf{P}}^{(2)}\right)$, then we define V^{ε}_{ext} as the union of those Ω_k such that $s_k \geq \varepsilon$ and, finally, we find the value ε' such that $\left\|\tilde{\mathbf{P}}^{(2)} - \mathbf{P}^{(2)}_{V^{\varepsilon}_{ext}}\right\|$ is minimum, ($\|\cdot\|$ being a matrix norm). The set $V^{\varepsilon'}_{ext}$, corresponding to ε', is taken as V_{ext}. It is worth noting that it is no longer guaranteed that $V \subseteq V_{ext}$.

Similarly, to compute V_{int} we associate to each $\Omega_k \subseteq V_{ext}$ the number $t_k = f\left(\tilde{\mathbf{P}}^{(2)} - \mathbf{P}^{(2)}_{V_{ext} \backslash \Omega_k}\right)$, then we define V^{ε}_{int} as the union of those $\Omega_k \subseteq V_{ext}$ such that $t_k \leq 1 - \varepsilon$ and, finally, we find the value ε'' such that $\left\|\tilde{\mathbf{P}}^{(2)} - \mathbf{P}^{(2)}_{V^{\varepsilon}_{int}}\right\|$ is minimum, ($\|\cdot\|$ being a matrix norm). The set $V^{\varepsilon''}_{ext}$, corresponding to ε'', is taken as V_{int}. Also in this case, it is no longer guaranteed that $V_{int} \subseteq V$ but only the obvious condition $V_{int} \subseteq V_{ext}$. Here we call the first test (to exclude the pixels), test 1 and the second test (include pixels), test 2. The algorithm for tests 1 and 2 are shown in pseudo code of algorithms 3 and 4.

The efficiency of this inversion algorithm is high: it requires the computation of a number of matrices $\mathbf{P}^{(2)}_S$, where S is Ω_k or $V_{ext} \backslash \Omega_k$, and the eigenvalues for computing the sign indices s_k and t_k. The number of matrices $\mathbf{P}^{(2)}_S$ to be computed is proportional to the number of elements (the number of Ω_k's) of the subdivision of the domain Ω_c. Moreover, the computation of $\mathbf{P}^{(2)}_S$ is very efficient because it corresponds to the solution of an elliptic problem but in a bounded domain that can be described by a sparse matrix. On the contrary, the direct problem (calculation of the trans-impedance matrix) involve either a differential formulation in an unbounded domain associated to a sparse stiffness matrix, or an integral formulation defined on the region occupied by the materials and associated to a fully populated stiffness matrix.

```
Data: Measurement data
Result: Classification of the pixels
Test 1. Consider all $N$ pixels labeled 1 to $N$ .;
for k = 1 : N ;
Compute the second order moments by performing the forward solution with only $\eta_k$ equal to $\eta_S$ (other resistivity equal to $\eta_B$) in multiple frequency;
Compute and store the sign index $s_k$ ;
end;
Consider all distinct values of the stored sign index;
Classify the resistivity image using threshold $1 - \epsilon_1 = sk$;
Select the classified resistivity image with the smallest error;
The result is a set of pixels which are definitely part of the background, that is $V_2$, and a set which contains the inclusion but may also contain background, that is $V_{Ext}$.;
```

Algorithm 3: Monotonicity method, first test

```
Data: Measurement data
Result: Classification of the pixels
Test 2. Consider only pixels which are definitely not part of the background, that is the set $V_{Ext}$ from Test 1, with pixels labeled 1 to T.;
for k = 1 : T;
Compute the second order moments by performing the forward solution with $\eta_k$ equal to $\eta_B$ and other resitivities in $V_{Ext}$ equal to $\eta_S$, and other resistivities equal to $\eta_B$;
Compute and store the sign index $t_k$ ;
end;
Consider all distinct values of the stored sign index;
Classify the pixels in $V_{Ext}$ using threshold $1 - \epsilon_1 = t_k$;
(other pixels classified as background from Test 1);
Select the classified resistivity image with the smallest error;
The result is a set of pixels which are definitely part of the inclusion, that is $V_1$.;
```

Algorithm 4: Monotonicity method, second test

3.5. Time-varying model and inverse solver based on the linearized Kalman filter.

3.5.1. Formulation of the time-varying model. We consider the inverse problem as a state estimation problem to estimate the time-varying material distribution. Suppose that a measurement has been made at time t_k and that the information it provides is to be applied in updating the estimate of the state of a system at time t_k. It is also assumed that the problem has been discretized with respect to the time variable. In the state estimation problem, we need the so-called time-varying model which consists of the state equation (the temporal evolution of the conductivity distribution) and the measurement equation (the relationship between the conductivity distribution and voltages on the boundary). In general, the temporal evolution of the material distribution p_k in the object Ω is assumed to be of the linear form

$$p_{k+1} = F_k\, p_k + w_k \tag{52}$$

where $F_k \in \mathbb{R}^{N \times N}$ is the state transition matrix at time t_k and N is the number of states (conductivity distribution). Usually there is no *a priori* information on the time evolution of the conductivity distribution so that we take $F_k \equiv I_N$ (the identity matrix) for all t_k, to obtain the so-called random-walk model. It is assumed that w_k is white Gaussian noise with the following known covariance matrix $\Gamma_k^w \in \mathbb{R}^{N \times N}$,

$$\Gamma_k^w \equiv E\left[w_k\, w_k^T\right] \tag{53}$$

which determines the rate of time evolution in the conductivity distribution.

Next, consider the observation model. Let $Y_k \in \mathbb{R}^L$, defined as

$$Y_k \equiv \left[Y_{1,k}, Y_{2,k}, \ldots, Y_{L,k}\right]^T \tag{54}$$

be the voltages measured by the k-th excitation pattern. Then the relationship between the conductivity distribution and measured voltages can be described by the following nonlinear mapping with measurement error

$$Y_k = U_k(\sigma_k) + v_k \tag{55}$$

where the measurement error $v_k \in \mathbb{R}^L$ is assumed to be white Gaussian noise.

Linearizing (55) about the nominal value (best conductivity value) p_0, we obtain

$$Y_k = U_k(\sigma_0) + J_k(\sigma_0) \cdot (p_k - p_0) + \text{H.O.Ts} + v_k \tag{56}$$

where H.O.Ts represents the higher-order terms which are assumed to be additional white Gaussian noise, and $J_k(p_0) \in \mathbb{R}^{L \times N}$ is the Jacobian matrix defined by

$$J_k(p_0) \equiv \left.\frac{\partial U_k}{\partial p}\right|_{p=p_0}. \tag{57}$$

Let us define a pseudo-measurement as

$$y_k \equiv Y_k - U_k(p_0) + J_k(p_0) \cdot p_0 \tag{58}$$

then we obtain the following linearized measurement equation as

$$y_k = J_k(p_0) \cdot p_k + \bar{v}_k \tag{59}$$

where $\bar{v}_k \in \mathbb{R}^L$ is assumed to be composed of the measurement and linearization errors with the following known covariance as

$$\Gamma_k \equiv E\left[\bar{v}_k\, \bar{v}_k^T\right]. \tag{60}$$

3.5.2. Inverse solver based on the linearized Kalman filter. In Kalman filtering approach we estimate the state vector σ_k on the basis of a measurement taken up to the time t_k. With the Gaussian assumptions the required estimate is obtained by minimizing the cost functional which is formulated on the basis of the above state and measurement equations (52) and (59), respectively. The cost functional for the linearized Kalman filter (LKF) is of the form

$$\Xi(p_k) = \frac{1}{2}\left[\|p_k - p_0\|_{C_k^{-1}} + \|y_k - J_k(p_0) \cdot p_k\|_{\Gamma_k^{-1}}\right] \tag{61}$$

where $\|x\|_A$ denotes $x^T A x$, and $C_k \in \mathbb{R}^{N \times N}$ is the error covariance matrix, which is defined by

$$C_k \equiv E\left[(p_k - p_0)\,(p_k - p_0)^T\right]. \tag{62}$$

The two norms on the right-hand side in (61) refer to the weighted norms, having the inverse of the given covariances as weighting matrices.

By minimizing the cost functional (61), we can obtain the recursive linearized Kalman filtering algorithm. The basic steps of the computational procedure for the Kalman estimator are as follows [22] , [23]:

- time updating (prediction)

$$C_{k|k-1} = F_{k-1}\, C_{k-1|k-1}\, F_{k-1}^T + \Gamma_{k-1}^w \tag{63}$$

$$p_{k|k-1} = F_{k-1}\, p_{k-1|k-1} \tag{64}$$

- measurement updating (filtering)

$$G_k = C_{k|k-1}\, J_k^T \left(J_k\, C_{k|k-1}\, J_k^T + \Gamma_k\right)^{-1} \tag{65}$$

$$C_{k|k} = (I_N - G_k\, J_k)\, C_{k|k-1} \tag{66}$$

$$p_{k|k} = p_{k|k-1} + G_k \left(y_k - J_k\, p_{k|k-1}\right). \tag{67}$$

Hence, we can find the estimated state vector $p_{k|k} \in \mathbb{R}^N$ for the true state vector p_k in a recursive minimum mean square error sense. The Kalman gain matrix $G_k \in \mathbb{R}^{N\times L}$ in (65) does not depend on the state vector, because the Jacobian matrix only depends on the nominal value p_0 in (57). Therefore, it is possible to pre-compute the error covariance extrapolation (63), Kalman gain matrix (65), and error covariance update (66) off-line and store the Kalman gain matrix for minimizing the on-line computational time.

A striking feature is that the Kalman filtering technique is an on-line recursive form in place of the off-line batch form of the Newton-Gauss method. This eliminates the need to store past measurements in order to estimate the present state.

4. Numerical results

In this section we are presenting some numerical results that show some advancements in various imaging modalities. First we choose a simple numerical example in MIT to illustrate the reconstruction procedure. The true and reconstructed conductivity values for 20 unknowns (grouping elements to generate only 20 unknowns) can be seen in Fig. 4 for noise free data. The number of unknowns are small so as expected the inverse solver can reconstruct all 20 values with a good accuracy, and the quantitative reconstruction degrades when 2 percent Gaussian noise (2 percent of the average of measured data) was added to the simulated data (see Fig. 4). It is worth mentioning that in this example the same mesh was used to solve the forward problem as well as the inverse problem. Figure 5 show the reconstruction of three copper bars, diameter 19 mm each and an aluminum bar diameter 12.5 mm. The test was carried out by experimental MIT system and four bars were located in four corner of the imaging area. For MPT results, we inserted two bars with a relative permeability of 4 into the cylinder as a test phantom (see figure 6.a), and the background permeability is 3. Figure 6.b shows the reconstructed image from the test phantom of figure 6.a. Figure 6 is a cross section cylindrical region of interest for imaging. Figure 7 shows reconstructions for some situations with ECT data which have been used already earlier for a different reconstruction method in [83]. To evaluate the level set and pixel based algorithms, the experimental data was used from an 8 electrode sensor 84 mm in diameter. The measurement electrodes are 10 cm long (third direction) and are mounted symmetrically on the outside of an insulating pipe, and 28 measurement data are used the image and shape reconstruction. In the first example, a ring of Perspex with a circular object (Perspex 26 mm in diameter) in the centre is considered. In the second example two circular objects (Perspex 32 mm in diameter each) considered. The third example considers a single ring of Perspex with a circle in centre (air with diameter 26mm), and the fourth example one circular object (Perspex 32 mm in diameter) near the wall. All these inclusions are Perspex objects with relative permittivity of 1.8, and the background is free space with relative permittivity of 1.

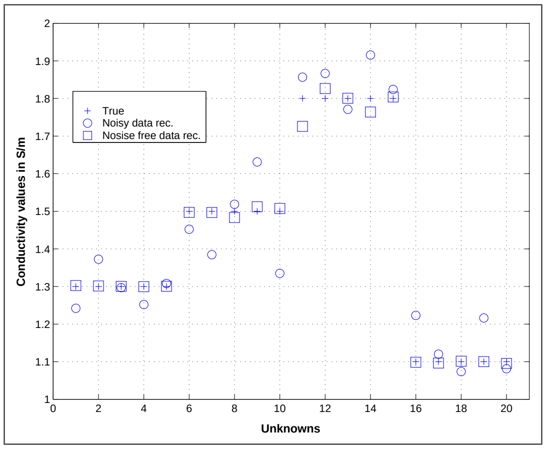

Figure 4: Reconstruction of 20 unknown using noise-free data and data with noise

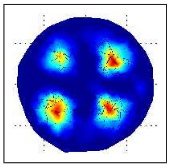

Figure 5: Reconstruction of three copper rods and one aluminum rod using experimental data of MIT

An annular shape object is a difficult task for high contrast MIT due to the screening effect of the eddy current. An experimental test example of an annular

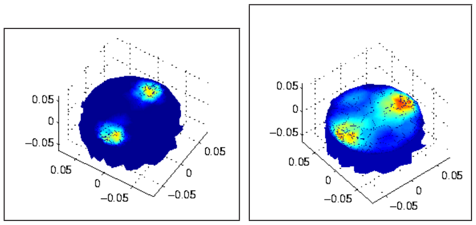

(a) (b)

Figure 6: Reconstruction of the test phantom in (a)True, (b), the image is a cross section of cylinder using simulated MPT data.

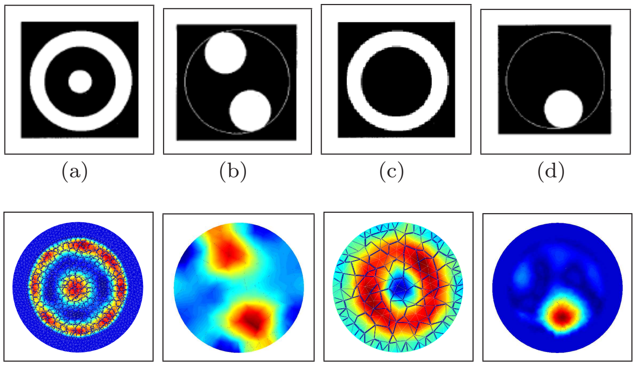
(a) (b) (c) (d)

(e) (f) (g) (h)

Figure 7: Reconstruction of plastic bar(s) and ring using regularized linear steps, permittivity 1.8 for plastic, figure (a) is a rod in centre, (b) a rod close to wall, (c) two rods close to wall and (d) a ring

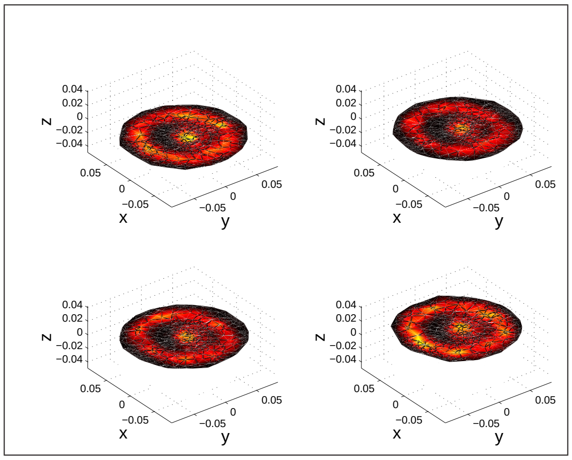

Figure 8: An annular object with the experimental data using metal object

object is presented here. Figure 8 shows reconstruction of an annually shape object with copper ring and rod using 8 nonlinear steps of regularized Gauss-Newton.

Figure 9, three big copper rods (19 mm in diameter) using experimental data and our level set method [70].

Figure 10 shows the reconstruction of three metal objects with radius 0.02 centred at (-0.05,-0.02) m and (-0.05,-0.03) m and a cylinder with radius 0.03 m centred at (0,0) m using our monotonicity method and multifrequency MIT data [69]. The gray area is that area that could not be classified either as background nor as inclusion. Monte Carlo Marko Chain (MCMC) algorithm was used in [5] to classify the pixels that can not be classified using monotonicity method.

Figure 11 shows 3D ERT reconstruction of true object with the result of excluding and including test. The ERT system here includes 32 electrodes. The

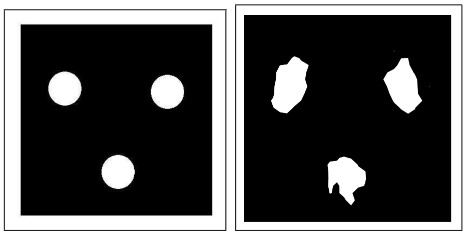
(a) (b)

Figure 9: (a): True object and (b): Level set reconstruction

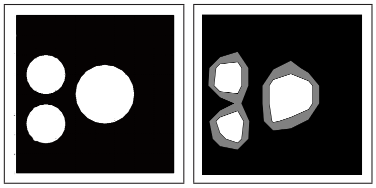
(a) (b)

Figure 10: Shape reconstruction of three object, (a): True object and (b): Monotonicity classification

background conductivity is 1 Sm^{-1} and the inclusion has conductivity 2 Sm^{-1}. The mesh was the simple mesh provided by EIDORS [47]

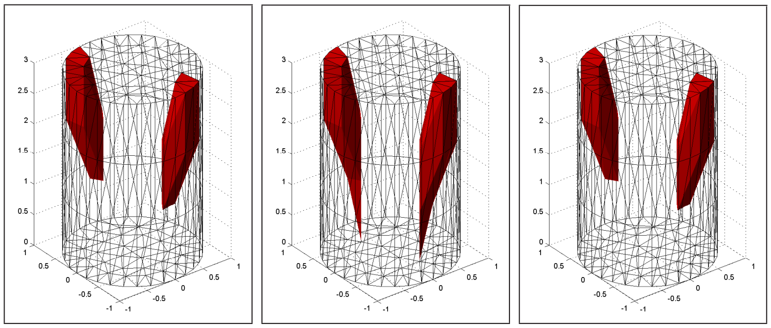

(a) (b) (c)

Figure 11: Example of monotonicity reconstruction in 3D ERT, (a): True shape, (b): First test and (c): second test

Figure 12 is a multifrequency image reconstruction by Patricia Brunner [12]. The method is based on frequency-differential, which is of high interest in motionless organs like the brain, where a state-differential method cannot be applied. An equation for frequency-differential MIT was derived taking into consideration the frequency dependence of the sensitivity matrix. The frequency-differential method shows a good localization of the perturbation.

An edge detection based regularization technique was applied by Raymon Casanova [13], in which the improvement has been made on detecting objects as it can be seen in experimental test of figure 13. Tikhonov regularization for the cases with strong discontinuities tends to produce blurred images. In [13] the performance of an edge-preserving regularization method, called ARTUR [14], is evaluated in the context of magnetic induction tomography (MIT). ARTUR is a deterministic method based on half-quadratic regularization, where complementary a priori information may be introduced in the reconstruction algorithm by the use of a nonnegativity constraint. Results show advantage of edge-preserving method to Tikhonov regularization.

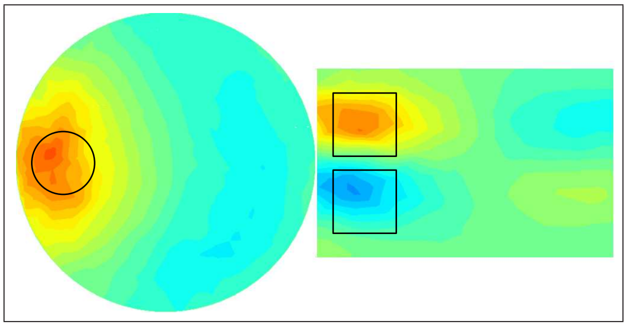

Figure 12: Frequency difference imaging in MIT reconstruction

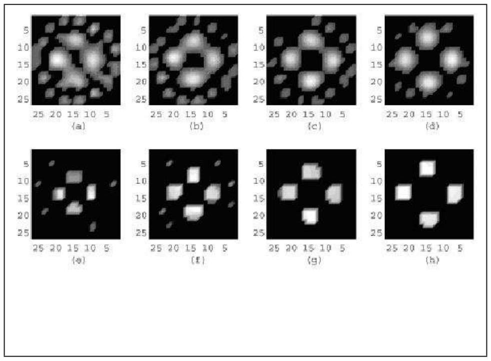

Figure 13: Reconstructed images of four objects with the same electrical conductivity (1 S/m) evenly distributed around the centre of the region of interest at a distance d from it: a) and e) 1.5 cm, b) and f) 2 cm, c) and g) 3 cm, d) and h) 4 cm. The first row concerns Tikhonov regularization and the second row ARTUR with nonnegativity constraining.

To show the linear Kalman filter we use an experimental example of MIT shown in figure 14. For each step, the bar is moved by half its radius. As can be seen the position of the bar can be clearly reconstructed for each step, despite the change in excitation. In the second example, the copper bar is moved towards the centre; this time in steps equal to the radius of the bar. Again the position of the bar can be distinguished.

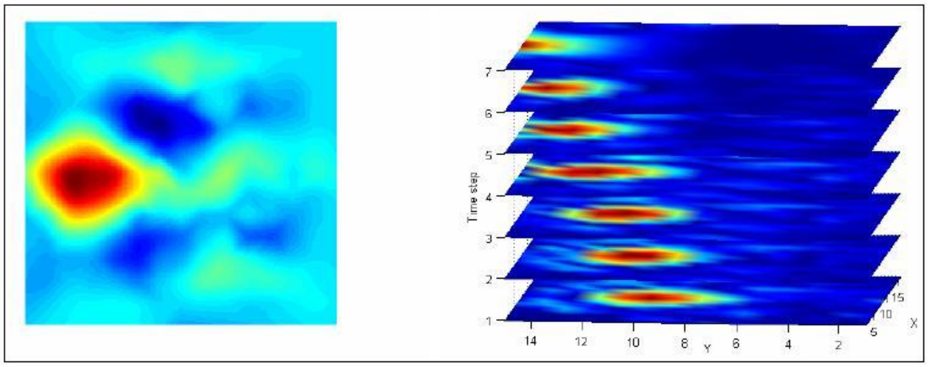

Figure 14: Reconstruction of a moving object by using the Kalman filter, left is the static image of a moving object and right is the temporal images

5. Discussion and future directions

Various image reconstruction methods have been reviewed for number of soft field tomography techniques. The paper gives an unified overview of different types of numerical methods for image reconstruction arising from electrical impedance tomography and magnetic induction tomography. The methods discussed are the linear methods, the nonlinear methods, the semi-linear methods, methods for discontinuous coefficients and methods that are based on a time-varying model.

The nonlinear inverse problem can be solved using regularized linear iterative steps and there are needs for more studies in the solution of linear system of equations arising in each nonlinear step. One can further explore efficient ways of regularization and especially the choice of the regularization parameter. Computational imaging in two and, in particular, three dimensions involve the processing of large amounts of data, and must be performed with algorithms suited for such large-scale problems. Hence there is a growing interest in iterative algorithms that only involve matrix-vector multiplications and thus avoid the high computational complexity of classical factorization algorithms. Another advantage of the iterative methods is that they only require the operation of the forward model on the iteration vectors, and they are matrix-free in the sense that they only require access to a computational module that produces the result of applying the forward operator to a vector. Hence the forward operator is not restricted to be a (sparse) matrix it can be a sophisticated model that involves, say, the solution of a partial differential equation. It is precisely these features and advantages of iterative methods that make them well suited for designing modular regularization algorithms which, in principle, can make use of any forward operator, as long as it is available as a computational module.

Application of the level set method and AMG for complex conductivity can be an interesting future study [59]. One needs to study further surface based (curve based) regularization schemes when using the level set method. Application of AMG in *curl curl* operator of magnetostatic and eddy current forward problem will be a very helpful tool to speed up the forward solvers. Use of TV regularized level set [17] is particulary an attractive method and could be used for real world application. One could study the simultaneous reconstruction of permeability and complex conductivity using MIT data. Similar to the optical tomography (recovering absorption and scattering coefficient) [3] some normalization is required to stabilize the inverse problem here. Adaptive multi-frequency excitation could be an interesting aspect in MIT, where sensors can be excited simultaneously but with differen frequencies. These frequency can be chosen so that they create the best distinguishability. Experimental validation of absolute value imaging can be an interesting next step [60]

The exterior boundary movement is a major source of error in many EIT applications such as thorax imaging. Simultaneous reconstruction of boundary movement and internal material distribution has been given in [62] and [35] using experimental data, which can reduce the artifact due to the surface movement. But in some application deformation of the exterior boundary could be a source of more independent data. When imaging a deformable media such as breast cancer monitoring, the electrodes could be located adaptively and be allowed to move. In addition registration techniques are required to track the location of the potential tumor while we deform the breast. Taking into account the mechanical properties of the object (here breast) is required in order to register the images from each movement. By relocating the electrodes (by deforming the media), one can generate multiple data set as well as the optimum data. For such a goal in EIT, we need to develop moving boundary forward solvers as well as tomographic software for moving objects. The adaptive location of the sensors (electrodes) is a nonlinear optimization problem, and far more challenging that adaptive excitation pattern.

This paper has focused on the development that are the bases for the modular imaging algorithms using the finite element method (FEM), which has specific applications in electrical impedance tomography and magnetic induction tomography. We suggest that by having modular inverse solvers we can choose between reconstruction algorithms and regularization schemes. It is known that each reconstruction method is able to detect some information regarding the object, so it could be an idea to have a main management software to make a decision on which reconstruction algorithm to be selected. To make it clear, here is a simple example. If we do not know if the material distribution is two phase or not, we may first use a pixel based reconstruction to recover the material distribution. By analyzing the information acquired from this step we may be able to deduce that the material was two phase, now better information can be extracted by using a shape based method.

This work is not a complete overview of all image reconstruction methods for low frequency electromagnetic imaging. It only covers certain aspects of the computational methods. There is still scop for further innovation and development in this area. For the forward problem, we may have to use more complicated modeling to account for more sources of the errors [77] or use more advanced approximation error models to compensate for the simplified models [2]. For the inverse problem, the mathematical modeling of the desired and meaningful solutions and modeling of meaningful regularization terms will be very important. It seems that the computational technology to play a key rule in further development of electrical and electromagnetic tomography. As a concluding remark, I would like to mention that the delay between an elegant algorithm developed by a mathematician and use of the algorithm in experimental set ups is very high. This gap could be filled by computational scientists and mathematical engineers.

Acknowledgements

I would like to thank Prof. WRB Lionheart for his helpful and inspiring discussions in inverse problems. I would also like to acknowledge the contribution of Prof. Tony Peyton and his colleagues who introduced us to (industrial) MIT and Prof. WQ Yang for fruitful discussion in ECT. I would like to thank my collaborators in past few years, Dr O Dorn, Dr N Polydorides, Dr A Tamburrino, Dr R Aykroyd, Dr R West, Dr CE Powell, Dr A Adler, Dr X Ma, Dr H Dehghani, Dr F Podd, Dr M Goharian, Dr B S Kim, and Mr C. Gomez-Laberge. Many thanks to MIT research group of Prof. A Korjenovsky, Prof. H. Scharfetter and Prof. H Griffiths and Mr M Bayers from PTL for providing me with some of their results and photos.

References

[1] R. Albanese and G. Rubinacci, *" Integral formulation for 3D eddy-current computation using edge elements*," IEE Proceedings, Vol. 135, Pt. A, No. 7, pp. 457-462, 1988.

[2] S. A. Arridge, J. P. Kaipio, V. Kolehmainen, M. Schweiger, E. Somersalo, T. Tarvainen and M. Vauhkonen, *"Approximation errors and model reduction with an application in optical diffusion tomography*" Inverse Problems 22 No 1, 175-195, 2006.

[3] S. R. Arridge, *"Topical review: Optical tomography in medical imaging,*" Inverse Problems 15(2), 41-93, 1999.

[4] S. R. Arridge and J. C. Hebden, *"Optical imaging in medicine:II. Modelling and reconstruction,*" Physics in Medicine and Biology, 42(5), 841-853, 1997.

[5] R. G. Aykroyd, M. Soleimani, and W. R. B. Lionheart, *"Conditional Bayes reconstruction for ERT data using resistance monotonicity information,*" Meas. Sci. Technol., 17, 2405-2413, 2006.

[6] D. C. Barber, and B. H. Brown, *"Imaging Spatial Distributions of Resistivity Using Applied Potential Tomography,*" Electronic Letters, 19:22, pp. 933-935, 1983.

[7] R. H. Bayford, *"Bioimpedance Tomography, Electrical Impedance Tomography,"* Review Annals Biomedical Engineering, vol. 8, 2006.

[8] R. Binns, A. R. A. Lyons, A. J. Peyton and W. D. N. Pritchard, *"Imaging molten steel flow profiles*," Meas. Sci. Technol., 12, 1132-1138, 2001.

[9] O. Biro, *"Edge element formulations of eddy current problems.*," Computer methods in applied mechanics and engineering, 169, 391-405, 1999.

[10] M. Brühl, *"Explicit Characterization of Inclusions in Electrical Impedance Tomography*," SIAM J Math Anal, 32, pp. 1327-1341, 2001.

[11] A. Bossavit, *"Computational Electromagnetism*," Academic Press (Boston), 1998.

[12] P. Brunner, R. Merwa, A. Missner, J. Rosell, K. Hollaus and H. Scharfetter, *"Reconstruction of the shape of conductivity spectra using differential multi-frequency MIT"*, Physiol. Meas. 27, 5, S237-S248, 2006.

[13] R. Casanova, A. Silva and A. R. Borges, *"MIT image reconstruction based on edge-preserving regularization*," Physiol. Meas., 25, 195-207, 2004.

[14] P. Charbonnier, L. Blanc-Feraud, G. Aubert and M. Barlaud, *"Deterministic edge-preserving regularization in computed imaging*", IEEE Trans. Image Process. 6, 298-311, 1997.

[15] M. Cheney, D. Isaacson, J. C. Newell, S. Simske and J. Goble, *"NOSER: An algorithm for solving the inverse conductivity problem*," Int. J. Imaging Systems & Technology 2, 66-75, 1990.

[16] M. Cheney, D. Isaacson and J. C. Newell, *"Electrical Impedance Tomography*," SIAM Review., 41(1), pp 85-101, 1999.

[17] E. T. Chung, T. F. Chan and X-C Tai, *"Electrical Impedance Tomography Using Level Set Representation and Total Variational Regularization,*" Journal of Computational Physics, vol 205, pp. 357-372, 2005.

[18] O. Dorn and D. Lesselier, *" Level set methods for inverse scattering,*", Inverse Problems, 22, 4 , R67-R131, 2006.

[19] D. N. Dyck, D. A. Lowther and E. M. Freeman, *" A Method of computing the sensitivity of the electromagnetic quantities to changes in the material and sources*," IEEE Trans. MAG., 3, 5, 3415-3418, 1994.

[20] K. Fujiwara, T. Nakata and H. Fusayasu, *"Accelelation of convergence characteristics of the ICCG method*," IEEE Trans. MAG, 29, 2, 1958-1961, 1993.

[21] P. A. Gaydecki, I. Silva, B. T. Fernandes and Z. Z. Yu, *"A portable inductive scanning system for imaging steel reinforcing bars embedded within concrete*," Sensors and Actuators A: Physical 84, pp. 25-32, 2000.

[22] A. Gelb, *" Applied Optimal Estimation*", (Massachusetts: The M.I.T. Press), 1974.

[23] M. S. Grewal and A. P. Andrews, *" Kalman Filtering: Theory and Practice, Using MATLAB*", (New York: John Wiley & Sons. Inc.), 2001.

[24] N. G. Gencer and M. N. Tek, *"Electrical conductivity imaging via contactless measurements*," IEEE Trans. on Medical Imaging, 18, 7, 617-627, 1999.

[25] H. Griffiths, W.R. Stewart and w. Gough W *"Magnetic induction tomography: Measurements with a single channel*," X-ICEBI, Barcelona, 361-364, 1998.

[26] H. Griffiths, *"Magnetic induction tomography*," Measurement Science and Technology, 12, 8, 1126-1131, 2001.

[27] J. Hadmard, 1923, *"Lectures on Cauchy's problem in linear partial differential equations,"* Yale University Press, New Haven, CT, 1923.

[28] P. C. Hansen, *"Rank-Deficient and Discrete Ill-Posed Inverse Problems*," SIAM, Philadelphia, PA., 1998.

[29] M. Hanke-Bourgeois and M. Brühl, *"Recent progress in electrical impedance tomography*," Inverse Problems, 19, pp. S65-S90, 2003.

[30] D. S. Holder, *" Electrical Impedance Tomography: Methods, History and Applications,"* Institute of Physics, ISBN 0750309520, 2004.

[31] H. Igarashi, K. Ooi and T. Honma, *"Magnetostatic permeability tomography*," Proc. COMPUMAG-Saratoga, CD-ROM, Paper Number 43142, 2003.

[32] K. Y. Kim, B. S. Kim, M. C. Kim, Y. L. Lee and M. Vauhkonen, *"Image reconstruction in time-varying electrical impedance tomography based on the extended Kalman filter*", Meas. Sci. Tech. **12** 1032–9, 2001.

[33] B. S. Kim, K. Y. Kim, T. J. Kao, J. C. Newell, D. Isaacson and G. J. Saulnier, *"Dynamic electrical impedance imaging of a chest phantom using the Kalman filter*", Physio. Meas., **27** S81–91, 2006.

[34] V. Kolehmainen, S. R. Arridge, W. R. B. Lionheart, M. Vauhkonen and J. P. Kaipio, *"Recovery of region boundaries of piecewise constant coefficients of an elliptic PDE from boundary data*," Inverse Problems, 15, pp. 1375-1391, 1999.

[35] V. Kolehmainen, M. Lassas and P. Ola, *" Inverse conductivity problem with an imperfectly known boundary,"* SIAM J. Appl. Math. 66 (2) 365-383, 2006.

[36] A. N. Kolmogorov and S. V. Fomin, *"Elements of rhe Theory of Funclions and Funcrional Analysis,"* (Rochester. NY: Graylock Press) 1957-61.

[37] A. V. Korjenevsky , V. A. Cherepenin and S. Sapetsky, *"Magnetic induction tomography: experimental realization*," Physiol. Meas., 21, 1, 89-94, 2000.

[38] A. V. Korjenevsky, V. A. Cherepenin, and S. A. Sapetsky, 2001, *"Visualization of electrical impedance by magnetic induction tomography*," in Proc. of the World Congress on Industrial Process Tomography, 240-246, 2001.

[39] A. V. Korjenevsky, *"Solving inverse problems in electrical impedance and magnetic induction tomography by artificial neural networks,"* Journal of Radioelectronics, 12, 2001.

[40] M. H. Loke and T. Dahlin, , *" A comparison of the Gauss–Newton and quassi–Newton methods in resistivity imaging inversion*," Journal of Applied Geophysics, 49, 149-162, 2002

[41] A. Litman, D. Lesselier and F. Santosa, *"Reconstruction of a two-dimensional binary obstacle by controlled evolution of a level-set*," Inverse Problems, 14, 685-706, 1998.

[42] X. Ma, A. J. Peyton, S. R. Higson, A. Lyons and S. J. Dickinson, *"Hardware and software design for an electromagnetic induction tomography (EMT) system for high contrast metal process applications ,*" Meas. Sci. Technol. 17, 1, 111-118, 2006.

[43] V. A. Morozov, 1984, *"Methods for solving incorrectly posed problems,"* Springer-Verlag, New York, 1984.

[44] J. C. Nedelec, *"Mixed finite elements in $R3$*," Numer. Math., 35, 315-341, 1980,

[45] J. C. Nedelec, *" A new family of mixed finite elements in $R3$*," Numer. Math., 50, 57-81, 1986.

[46] A. J. Peyton, Z. Z. Yu, S. Al-Zeibak, N. H. Saunders, and A. R. Borges, *"Electromagnetic imaging using mutual inductance tomography: Potential for process applications*," Part. Syst. Charact., 12, 68-74, 1995.

[47] N. Polydorides and W. R. B. Lionheart, *" A Matlab toolkit for three-dimensional electrical impedance tomography: a contribution to the Electrical Impedance and Diffuse Optical Reconstruction Software project*," Meas. Sci. Technol., 13, pp. 1871-1883, 2002.

[48] C. H. Riedel, M. Keppelen, S. Nani, R. D. Merges, and O. Dossel, *“Planar system for magnetic induction conductivity measurement using a sensor matrix,”* Physiol. Meas., 25, 1, 403-411, 2004.

[49] C. H. Riedel, *“Planare induktive Impedanzmessverfahren in der Medizintechnik,”* PhD thesis, Universitt Karlsruhe (TH), Institut fr Biomedizinische Technik, 2004.

[50] J. Rosell, R. Merwa, P. Brunner and H. Scharfetter, *“A multifrequency magnetic induction tomography system using planar gradiometers: data collection and calibration*”, Physiol. Meas. 27 No 5, S271-S280, 2006.

[51] F. Santosa, *“A Level-Set Approach for Inverse Problems Involving Obstacles*,” ESAIM: Control, Optimization and Calculus of Variations 1, 17-33, 1996.

[52] H. Scharfetter, H. K. Lackner and J. Rosell, *“High resolution hardware for magnetic induction tomography (MIT) at low frequencies*,” in Proc. of the EIT Conference in London, 2000.

[53] H. Scharfetter, H. K. Lackner and J. Rosell, *“Magnetic induction tomography: hardware for multi-frequency measurements in biological tissues*,” Physiol. Meas., 22, 1, 131–146, 2001.

[54] H. Scharfetter, P. Riu, M. Populo and J. Rosell, *“Sensitivity maps for low-contrast-perturbations within conducting background in magnetic induction tomography (MIT)*,” Physiol. Meas., 23: 195-202, 2002.

[55] H. Scharfetter, R. Casañas and J. Rosell, *“Biological Tissue Characterization by Magnetic Induction Spectroscopy (MIS): Requirements and Limitations*,” IEEE Trans. on Biomedical Engineering, 50, 7, 2003.

[56] H. Scharfetter, R. Merwa, and K. Pilz, *” A new type of gradiometer for the receiving circuit of magnetic induction tomography (MIT)*.” Physiol Meas 26, S307-S318, 2005.

[57] J. A. Sethian, *Level Set Methods and Fast Marching Methods*, (2nd ed) Cambridge University Press, 1999.

[58] M. Soleimani, W. R. B. Lionheart and O. Dorn, *”Level set reconstruction of conductivity and permittivity from boundary electrical measurements using experimental data*”, Inverse problems in science and engineering, 14, 2, 193-210, 2006..

[59] M. Soleimani, C. E. Powell and N. Polydorides, *“Improving the Forward Solver for the Complete Electrode Model in EIT using Algebraic Multigrid,”* IEEE Transaction on Medical Imaging, 24, 5, 577-583, 2005.

[60] M. Soleimani, W. R. B. Lionheart, *”Absolute conducitivty reconstruction in magnetic induction tomography using a nonlinear method*,” IEEE Trans. Med. Imaging. vol. 25, no.12, 1521-1530, 2006.

[61] M. Soleimani, W. R. B. Lionheart, *”Image reconstruction in three-dimensional magnetostatic permeability tomography*,” IEEE Transactions on Magnetics, 41, 4, 1274-1279, 2005.

[62] M. Soleimani, C. Gomez, A. Adler, *” Conductivity changes and electrode movement in electrical impedance tomography”*, Physio. Meas., 27, S103-S113, 2006.

[63] M. Soleimani, M. Vauhkonen, W. Q. Yang, A. J. Peyton, B. S. Kim and X. Ma, *”Dynamic imaging in electrical capacitance tomography and electromagnetic induction tomography using a Kalman filter,”* Meas. Science. Tech. 18 (11), pages: 3287-3294, 2007.

[64] M. Soleimani, W. R. B. Lionheart, AJ Peyton, and X Ma and S Hugison, *“A 3D inverse finite element method applied to the experimental eddy current imaging data*, IEEE T MAG., 42, 5, 1560-1567, 2006.

[65] M. Soleimani, *“Sensitivity maps in three-dimensional magnetic induction tomography*”, Insight, Non-Destructive Testing and Condition Monitoring, 48, 1, 39-44, 2006.

[66] M. Soleimani, W. R. B. Lionheart, *“Nonlinear image reconstruction in electrical capacitance tomography using experimental data,”* Meas. Sci. Technol., 16, 1987-1996, 2005.

[67] M. Soleimani, *”Numerical modelling and analysis of the forward and inverse problems in electrical capacitance tomography*”, International Journal for Information and Systems Sciences, 1, 2, 193-207, 2005.

[68] M. Soleimani, and A. Movafeghi, *” A Shape Reconstruction Method for Electrical Resistance Tomography for Two Phase Materials,*” The Int. J. of Sci. Res. (IJSR) vol.16, 171-176, 2006.

[69] M. Soleimani, A. Tamburrino, *”Shape Reconstruction in Magnetic Induction Tomography Using Multifrequency Data,*” International Journal for Information Systems Sciences, 2, 3, 343-353, 2006.

[70] M. Soleimani, *”A Level Set Method Applied to Magnetic Induction Tomography Using Experimental Data*”, Research in Nondestructive Evaluation (RNDE), 18,1, 1-12, 2007.

[71] E. Somersalo, D. Isaacson and M. Cheney, *“A linearized inverse boundary-value problem for Maxwell equation*,” J comp appl math., 42, 123-136, 1992.

[72] E. Somersalo, D. Isaacson and M. Cheney, *"Existence and uniqueness for a electrode models for electric current computed tomography*," SIAM Journal of Applied Mathematics, 52, 1023–1040, 1992.

[73] N. Soni, K. D. Paulsen, H. Dehghani, and A. Hartov, *"Finite Element Implementation of Maxwell's Equations for Image Reconstruction in Electrical Impedance Tomography*", IEEE Trans. Med. Img. 25(1), 55-61, 2006.

[74] A. Tamburrino, G. Rubinacci, M. Soleimani, W. R. B. Lionheart, *A Noniterative Inversion Method for Electrical Resistance, Capacitance and Inductance Tomography for Two Phase Materials*, In Proc. 3rd World Congress on Industrial Process Tomography, The Rockies, Alberta, Canada, 2003.

[75] A. Tamburrino and G. Rubinacci, *"Fast Methods for Quantitative Eddy-Current Tomography of Conductive Materials* ", IEEE T Magn, 42, 8, 2017- 2028, 2006.

[76] A. Tamburrino and G. Rubinacci, *"A new non-iterative inversion method in electrical resistance tomography*," Inverse Problems, 18, 1809-1829, 2002.

[77] A. Tizzard and R. Bayford, *" Improving the finite element forward model of the human head by warping using elastic deformation*", Physiol. Meas. 28 No 7, S163-S182, 2007.

[78] M. Vauhkonen, P. A. Karjalainen and J. P. Kaipio, 1998 *"A Kalman filter approach to track fast impedance changes in electrical impedance tomography*", IEEE Trans. Biomed. Eng. **45** 486–93, 1998.

[79] S. Watson, R. G. Williams, H. Griffiths, W. Gough, and A. Morris, *"Frequency downconversion and phase noise in MIT*," Physiol. Meas., 23, 189-194, 2002.

[80] S. Watson, R. G. Williams, H. Griffiths, W. Gough, and A. Morris, *" Magnetic induction tomography: phase versus vector-voltmeter measurement techniques*," Physiol. Meas., Vol. 24, 555-564, 2003.

[81] H. Whitney, *"Geometric Integration Theory*," Princeton University Press, 1957.

[82] W. Q. Yang and L. H. Peng, *" Image reconstruction algorithms for electrical capacitance tomography,*" Meas. Sci. Technol. (Review Article), 14, pp. R1-R13, 2003.

[83] W. Q. Yang, D. M. Spink, T. A. York and H. McCann, *"An image-reconstruction algorithm based on Landweber's iteration method for electrical-capacitance tomography*," Meas. Sci. Technol., 10, pp. 1065-1069, 1999.

[84] W. Yin, A. J. Peyton, G. Zysko and C. Ktistis, *"Evaluation of the radiative wave propagation effect in EMT,*" Int. J Information and Systems Sciences, Special Issue on Computational Aspects of Soft Field Tomography, vol. 2, no. 4, 575-584, 2006.

Department of electronics and electrical engineering, the University of Bath, UK
E-mail: `manuchehr.soleimani@bath.ac.uk`